Title: Alternate splice variants of the mitochondrial fission protein *DNM1L*/Drp1 regulate mitochondrial dynamics and cell fate in ovarian cancer.

Authors: Zaineb Javed[1,2], Dong Hui Shin[2,β], Weihua Pan[1], Sierra R. White[1], Yeon Soo Kim[2,χ], Amal Taher Elhaw[1,2], Shriya Kamlapurkar[1], Ya-Yun Cheng[1], J Cory Benson[3], Ahmed Emam Abdelnaby[3], Rebecca Phaeton[4,δ], Hong-Gang Wang[5], Shengyu Yang[6], Mara L.G. Sullivan[7], Simon C. Watkins[7], Steven J. Mullett[3, 8], Stacy L. Gelhaus[3, 8], Nam Lee[9], Lan G. Coffman[1], Katherine M. Aird[3], Mohamed Trebak[3,10], Karthikeyan Mythreye[11], Vonn Walter[12], Nadine Hempel[1,α]

[1] Department of Medicine, Division of Hematology/Oncology, UPMC Hillman Cancer Center, University of Pittsburgh School of Medicine, PA, USA

[2] Department of Pharmacology, College of Medicine, Pennsylvania State University, Hershey, PA, USA

[3] Department of Pharmacology and Chemical Biology, University of Pittsburgh School of Medicine, PA, USA

[4] Department of Obstetrics & Gynecology, College of Medicine, Pennsylvania State University, Hershey, PA, USA

[5] Department of Pediatrics, College of Medicine, Pennsylvania State University, Hershey, PA, USA

[6] Department of Cellular and Molecular Physiology, College of Medicine, Pennsylvania State University, Hershey, PA, USA

[7] Center for Molecular Imaging, University of Pittsburgh School of Medicine, PA, USA

[8] Health Sciences Mass Spectrometry Core, University of Pittsburgh, PA, USA

[9] Division of Pharmacology, Chemistry and Biochemistry, College of Medicine, University of Arizona, Tucson, AZ, USA

[10] Vascular Medicine Institute (VMI), University of Pittsburgh School of Medicine, PA, USA

[11] Department of Pathology and O'Neal Comprehensive Cancer Center, Heersink School of Medicine, University of Alabama at Birmingham, Birmingham, AL, USA

[12] Department of Public Health Sciences, Division of Biostatistics and Bioinformatics and Department of Biochemistry and Molecular Biology, College of Medicine, Pennsylvania State University, Hershey, PA, USA

[α]Corresponding Author:
University of Pittsburgh School of Medicine, Division of Hematology/Oncology
UPMC Hillman Cancer Center
The Assembly, Rm 2039
5051 Centre Ave, Pittsburgh, PA 15213
Ph: 412-648-4822
nah158@pitt.edu

Current Address:
[β] School of Pharmacy, Virginia Commonwealth University, Richmond, VA, USA
[χ] Division of Human Biology, Fred Hutchinson Cancer Center, Seattle, WA, USA
[δ] GlaxoSmithKline, Collegeville, PA, USA

Abstract

Aberrant mitochondrial fission/fusion dynamics have previously been reported in cancer cells. While post translational modifications are known regulators of GTPases of the mitochondrial fission/fusion machinery, we show for the first time that alternate splice variants of the fission protein Drp1 (*DNM1L*) have specific and unique roles in ovarian cancer, adding to the complexity of mitochondrial fission/fusion regulation in tumor cells. We find that ovarian cancer specimens express a Drp1 alternate splice transcript variant lacking exon 16 of the variable domain. High expression of Drp1 lacking exon 16 relative to other transcripts is associated with poor patient outcome. Unlike the full length variant, expression of Drp1 lacking exon 16 leads to decreased association of Drp1 to mitochondrial fission sites, more fused mitochondrial networks, enhanced respiration and TCA cycle metabolites, and is associated with a more tumorigenic phenotype. These effects can also be reversed by specific siRNA-mediated inhibition of the endogenously expressed transcript lacking exon 16. Moreover, lack of exon 16 abrogates mitochondrial fission in response to pro-apoptotic stimuli and leads to decreased sensitivity to chemotherapeutics. These data emphasize the significance of the pathophysiological consequences of Drp1 alternate splicing and divergent functions of Drp1 splice variants, and strongly warrant consideration of Drp1 splicing in future studies.

Introduction

Mitochondria are highly dynamic organelles continuously undergoing fission and fusion events to facilitate adaptations to cellular and extracellular cues. The opposing processes of mitochondrial fission and fusion are mediated by several evolutionarily conserved dynamin-related GTPases, including Mitofusins (Mfn1&2) and Opa1 which promote fusion and Dynamin-related Protein 1 (Drp1) which mediates mitochondrial fission [1, 2]. Drp1, which is encoded by the gene *DNM1L*, forms homo-multimeric helical structures around the outer mitochondrial membrane to initiate division, and is tightly regulated by post-translational modifications, oligomerization and interaction with proteins that anchor Drp1 to mitochondria [3-7]. Given that the shape of mitochondria are inextricably linked to their function, maintaining a balance between these dynamic fission and fusion events is essential in preserving mitochondrial respiration, and for the proper distribution of mitochondria and mitochondrial DNA during mitosis [8, 9]. Moreover, mitochondrial fission is also an integral component of the apoptotic and mito/autophagy pathways [10, 11]. Perturbation in mitochondrial fission/fusion dynamics have been implicated in cancer, and cancer cells can exploit adaptive mitochondrial dynamics to their advantage for meeting their heightened energy demands and to regulate cellular processes including tumor metabolism, stress response pathways and resistance to apoptosis. Several studies have described a role for enhanced fission in cancer [12-14], and this shown to be associated with cell cycle progression [15, 16] and migration [17]. Underlying genetic factors may also contribute to exacerbated signaling that drives the activation of fission, as observed in BRAF and KRAS mutant tumors where Drp1 phosphorylation of S616 is activated via Erk [13, 14, 18]. On the contrary, mitochondrial fission is associated with apoptosis and decreased fission can result in apoptosis resistance [11, 19-21]. Enhanced fusion may thus be one mechanism by which tumors evade apoptosis in response to chemotherapeutic agents [22, 23]. These seemingly conflicting studies appear to suggest that both aberrant fission and fusion could have important roles during tumor progression and that the dysregulation of mitochondrial fission and fusion dynamics has the potential to influence various aspects of cancer, including progression, recurrence, and chemoresistance.

In addition to regulation by post-translational mechanisms, alternative splicing of the *DNM1L* pre-mRNA transcript has been shown to give rise to Drp1 splice variants with differential tissue expression, subcellular localization and fission activity [24-29]. However, despite the established importance of Drp1 as an integral mitochondrial fission protein few studies have investigated the expression and unique functions of Drp1 splice variants in pathophysiological contexts. The current study builds on our observations that ovarian cancer cell lines display

heterogeneous mitochondrial fission along with corresponding variations in Drp1 protein expression [30]. While Drp1 has been shown to be overexpressed in several tumor types, the role of individual splice variants was not considered in these studies. In ovarian cancer *DNM1L* gene amplification has been associated with poor patient outcomes [12, 31]. However, it is unclear how this reflects the relative expression and function of Drp1 splice variants. Here, we show for the first time that transcripts arising from exon 16 splicing are highly expressed in ovarian cancer cells and that relative expression of this transcript to full length Drp1 mRNA is predictive of poor patient outcome. Relative to the most studied Drp1 transcript that includes all exons, we demonstrate that exon 16 splicing results in a Drp1 protein with a unique function related to regulation of mitochondrial architecture, mitochondrial function, tumor metabolism and chemosensitivity in tumor cells. This represents the first study demonstrating the pathophysiological relevance of Drp1 splice variants.

Results

Ovarian cancer cells display distinct Drp1/*DNM1L* splice variant expression.

We previously observed that ovarian cancer cell lines express several different molecular weight protein variants of Drp1 [30]. To determine the clinical significance of this observation, Drp1 protein expression was assessed in ascites-derived epithelial ovarian cancer (EOC) cells from ovarian cancer patients (Fig. 1a). Four bands ranging in molecular weight between ~75- 85kDa were detected, with two being more prominently expressed, and the propensity for the lower molecular weight band of these to be present in samples of high grade serous ovarian adenocarcinoma (HGSA: ECO7, EOC14, EOC15 (Fig. 1a). Similarly, two major Drp1 protein bands were also observed in OVCA420 and OVCA433 ovarian cancer cells lines and these validated as being Drp1 using siRNA mediated knock down (Fig. 1b). Several Drp1/*DNM1L* transcript variants are annotated on the RefSeq record, including alternate splicing of exons 3, 16 and 17 [7, 27, 28, 32, 33]. To determine if the observed Drp1 protein variants are due to alternate start site utilization, splicing or alternate transcriptional termination, 5' and 3' rapid amplification of cDNA ends (RACE) was carried out. 3'RACE revealed that ovarian cancer cells express multiple Drp1 transcripts, including alternate splicing of exons 16 and 17, differential 3'UTR lengths, and identification of short transcripts that terminate after exon 14 (ΔC-Ex14) and in intron 17 (ΔC-In17) at predicted alternate polyadenylation sites (Fig. 1c, d and Extended Data Fig. 1a, c). 5'RACE demonstrated utilization of the same transcriptional start site and a lack of exon 3 for all transcripts (Extended Data Fig. 1b, c). The ΔC-In17 transcript displayed alternate splicing of exon 16 and had a predicted alternate stop codon within intron 17, leading to a

transcript with a novel coding sequence for 16 amino acids derived from intron 17 (Extended Data Fig. 1c, d). It is predicted to express a 65 kDa protein lacking the C-terminal GED domain (Fig. 1d, e), and using a polyclonal antibody, we were able to detect a protein at the predicted size which was decreased in expression following siRNA mediate Drp1 knock-down (Extended Data Fig. 1g). This could not be detected when using a monoclonal antibody targeting the C-terminus (Fig. 1b and Extended Data Fig. 1f), suggesting that the ΔC-In17 transcript may result in expression of a truncated protein. ΔC-In17 was detected to variable degrees in other ovarian cancer cell lines and patient derived tumor cells by RT-PCR (Extended Data Fig. 1e, and Extended Data Fig. 3a). While the functional consequences of this novel C-terminal truncation transcript require further study, annotation of TCGA ovarian cancer data for the ΔC-In17 transcripts demonstrated that these were only detected in <15% of TCGA ovarian cancer specimens (Fig. 2a). Thus, we focused on alternate splice variants of the variable domain exons 16 and 17 in full length Drp1, as these are predicted to yield proteins of molecular weights between 78-82kDa, matching the major protein variants observed in patient ascites derived EOCs (Fig. 1a, b). Exons 16 and 17 are located in the variable B-domain of Drp1 (Fig. 1e) and alternate splicing of these exons was further examined using RT-PCR with primers flanking the variable domain. Variable expression of splice variants was found in a panel of ovarian cancer cell lines (Fig. 1f), with the HGSA cell lines OVCAR3, OVCA420 and OVCA433 demonstrating a higher relative expression of the transcript with exon 16 spliced out, referred here after as Drp1(-/17).

Patient ascites derived epithelial ovarian cancer cells and tumor specimens display high expression of Drp1 transcript variants lacking exon 16, which is associated with poor patient outcome.

By annotating TCGA RNA sequencing data for the identified Drp1/*DNM1L* transcript variants we found that all variable domain (Exons 16 and 17) splice variants of the full-length transcripts were expressed to varying degrees in TCGA specimens (Fig. 2a, b). Of the four variable domain variants, highest levels of Drp1(-/17), the transcript lacking exon 16, was observed, followed by Drp1(16/17) and Drp1(-/-) displaying approximately equal expression (Fig. 2b). Drp1(16/-), the transcript lacking exon 17, was least abundant. Similar to our findings in cell lines, most Drp1/*DNM1L* transcripts in TCGA specimens lacked exon 3 (Extended Data Fig. 2a), agreeing with previous work describing exon 3 retention to be predominant in neuronal tissues [27]. TCGA data were independently validated by assessing splice variant transcript abundance in EOCs isolated from patient ascites (Fig. 2c) and in a separate cohort of matched

normal fallopian and omental or ovarian tumor specimens (Fig. 2d). Ascites-derived EOCs classified as HGSA and carcinosarcoma demonstrated predominant expression of the splice variant lacking exon 16, Drp1(-/17), and transcripts containing both exons 16 and 17, Drp1(16/17). The majority of matched samples displayed an increase in relative Drp1(-/17) expression in ovarian tumors (11/13 specimens) and omental tumors (5/5) compared to benign/normal fallopian tube (Fig. 2d; Extended Data Fig. 3). These data demonstrate that ovarian cancer cells express several Drp1/*DNM1L* splice variants, with a high abundance of Drp1(-/17) expression, suggesting that splicing of exon 16 and retention of exon 17 might be of significance to ovarian cancer.

We were curious if predominance of Drp1 splice variant expression is predictive of patient outcome. While patients with high expression of Drp1(-/17) trended towards worse overall survival (Fig. 2e), comparisons between high and low expression of individual Drp1 splice variants was not able to significantly predict survival (Extended Data Fig. 2b). However, grouping patients into mutually exclusive high vs low expression of splice variant pairs based on median expression cut-offs, revealed that relative abundance of the different variable domain splice variants influenced patient outcome (Fig. 2f; Extended Data Fig. 2c, d). Patients with tumors displaying high Drp1(-/17) and low Drp1(16/17) expression demonstrated poor overall survival compared to those with high Drp1(16/17) and low Drp1(-/17) expression (HR: 1.81, 95% CI: 1.076 to 3.071, log rank p=0.0208), with a median survival difference of 14.3 months (Fig. 2f). High Drp1(-/17):low Drp1(16/-) expression also decreased median survival by 11.7 months, albeit not significantly (HR: 1.508, 95% CI: 0.9304 to 2.444, log rank p=0.088), and other mutually exclusive expression comparisons between Drp1 splice variants were not significantly predictive of survival (Extended Data Fig. 2d). Although Drp1(16/17) and Drp1(-/17) transcript variants are both abundant in ovarian cancer cell lines and patient specimens, the above data suggest that their relative expression has consequences on ovarian cancer progression. Yet, the significance of exon 16 splicing on Drp1 function in cancer cells remains unexplored.

Loss of Exon 16 abrogates association with mitochondrial fission puncta and leads to more fused mitochondrial networks.

The HGSA OVCA433 cell lines was chosen as a model for subsequent studies as it displayed similar *DNM1L* variable domain transcript expression as HGSA patient specimens, while SKOV3 cells were chosen as a model due to their relatively equal expression of all four full length variable domain variants. To investigate their function, Drp1 splice variants were

expressed as GFP fusion proteins by lentiviral transduction in both cell lines (Fig. 3a and Extended Data Fig. 4a). Drp1(16/17) which contains exons 16 and 17 was localized in both the cytosol and at distinct mitochondrial fission puncta, as previously described by numerous Drp1 overexpression studies [6, 27, 34]. On the contrary, Drp1(-/17) co-localized less with mitochondria, with fewer distinct fission puncta observed. Instead, Drp1(-/17) displayed a filamentous pattern of localization (Fig. 3b). Consistent with the work by Strack and Cribbs, who demonstrated that the splicing of exon 16 modifies the association of Drp1 with mitochondria and increases binding to microtubules [27], we found that Drp1(-/17) exhibited co-localization with tubulin in ovarian cancer cells (Fig. 3b,c and extended Data Fig. 4b,c).

The expression of Drp1(-/17) was previously reported to lead to more fused and elongated mitochondrial network, likely due to the reduced association of Drp1(-/17) with mitochondria [27]. In line with this, compared to both GFP control and Drp1(16/17), cells expressing Drp1(-/17) had longer average mitochondrial branch lengths and a greater number of branches per mitochondria, indicative of a more interconnected mitochondrial network (Fig. 3d, and extended data Fig. 4d). In contrast, expression of Drp1(16/17) led to shorter branch lengths and fewer branches per mitochondria, a predicted phenotype following overexpression of Drp1 (Fig. 3d, Extended Data 4&5). TEM imaging additionally demonstrated elongated mitochondrial phenotypes in Drp1(-/17) expressing cells, contrasting with the smaller, more circular mitochondria seen following expression of Drp1(16/17) (Fig. 3e, f and Extended Data Fig. 4e and 5). Notably, expression of Drp1(-/17) led to an overall higher number and density of cristae per mitochondria (Fig. 3e, f and Extended Data Fig. 5).

After exposure to the pro-fission stimulus FCCP cells expressing Drp1(-/17) did not increase the number of Drp1 containing fission puncta as seen with expression of Drp1(16/17). Instead, Drp1(-/17) continued to exhibit high association with the microtubule network and mitochondria maintained their elongated mitochondrial morphology (Extended Data Fig. 6). These observations suggest that high expression of Drp1(-/17) could lead to abrogated mitochondrial fission and a more fused mitochondrial network, likely because of its lower association with mitochondrial fission puncta and partial localization to microtubules, and that cells expressing Drp1(-/17) have reduced response to pro-fission stimuli. These findings are significant, as Drp1(-/17) is highly expressed in tumor cells, yet past studies have primarily investigated the function of Drp1 in cancer cells by overexpressing the Drp1(16/17) variant transcript that includes both exons 16 and 17. Thus, we next investigated the functional consequences of Drp1(-/17) expression in ovarian cancer cells.

Expression of Drp1(-/17) increases oxygen consumption and alters tumor cell metabolism.

Due to their continuous membranes and matrix lumens, fused mitochondrial networks can facilitate better diffusion of molecules, including ADP, and reducing equivalents NADH and FADH2, necessary for oxidative phosphorylation [35, 36]. In addition, a more ordered cristae architecture improves electron transport chain super complex assembly, and these structural features have been associated with optimal mitochondrial respiration [37-39]. Given that Drp1(-/17) splice variant expression leads to enhanced mitochondrial networks and cristae numbers the effects on mitochondrial respiration and cellular metabolism were assessed. Using extracellular flux analysis significant increases in basal oxygen consumption rates (OCR), ATP-dependent OCR and spare respiratory reserve were observed between Drp1(-/17) and Drp1(16/17) expressing OVCA433 cells (Fig. 4a, b). An increase in OCR was similarly observed in SKOV3 cells expressing Drp1(-/17) (Extended Data Fig. 7). There were no differences in the expression of mitochondrial proteins COX-I (complex IV), and SDH-A (Complex II) following expression of either Drp1 variant suggesting that changes in mitochondrial activity are likely not attributable to changes in mitochondrial biogenesis (Extended Data Fig. 8a, b). In addition, no consistent changes in mitochondrial membrane potential or significant changes in mitoSox fluorescence, an indicator of mitochondrial oxidant production, were associated with the expression of either Drp1 variant in the cell lines tested (Extended Data Fig. 8c, d).

Compared to Drp1(16/17) or GFP controls, untargeted metabolomics (Fig. 4c) showed that cells expressing Drp1(-/17) also display an increase in metabolites linked to glycolysis and the pentose phosphate pathway. Related to the observed increases in lactate levels, an increase in extracellular acidification rate was also seen, although this was not significant in OVCA433 cells (Extended Data Fig. 7c-f). Select metabolites necessary for *de novo* purine and pyrimidine synthesis, such ribulose-5-phosphate, glycine and aspartate, and most TCA cycle metabolites were also elevated following overexpression of Drp1(-/17) relative to GFP control and Drp1(16/17) (Fig. 4c). These changes were also accompanied by elevated total NAD(H) levels and a decrease in the NAD+/NADH ratio (Fig. 4d and Extended Data Fig. 7g), which may be contributing to the reducing equivalents for increased respiration seen in Drp1(-/17) cells. Collectively, these findings suggest that enhanced Drp1(-/17) expression leads to an energetic phenotype and alters metabolism of ovarian cancer cells compared to cells expressing Drp1(16/17).

Drp1(-/17) expression is advantageous to the tumorigenic properties of ovarian cancer cells.

DNM1L gene amplification has been reported to correlate with cell cycle gene expression and poor patient outcomes in chemoresistant and recurrent ovarian cancer cases [12]. However, previous work did not account for expression of specific Drp1 splice variants, and it is thus unknown which Drp1 transcript variant is specifically associated with proliferation and chemoresistance. Considering that TCGA serous ovarian cancer patients with high Drp1(-/17) expression relative to low Drp1(16/17) expression exhibited a lower median overall survival, we further assessed the impact of Drp1 variable domain variant expression on tumor cell behavior. Clonogenicity assays demonstrated that Drp1(-/17) expression maintained high clonogenic potential similar to GFP controls, while expression of Drp1(16/17) was detrimental to single cell survival (Fig. 5a). Importantly, only Drp1(-/17) expression significantly increased the proliferation rate of both SKOV3 and OVCA433 (Fig. 5b). Cells expressing Drp1(-/17) notably also exhibited a strong increase in migration compared to GFP and Drp1(16/17) expressing cells (Fig. 5c). Taken together, these data show for the first time that expression of different Drp1 splice variants influences tumor cell behavior and that high expression of Drp1(-/17) compared to Drp1(16/17) is predominantly advantageous to ovarian cancer cells.

Drp1(-/17) protects cells against chemotherapy induced apoptosis.

Some studies have suggested that mitochondrial fission plays an integral part in the initiation of apoptosis[11, 19, 40], and Drp1(-/17) expression was previously shown to prevent staurosporin-mediated cell death[27]. We thus sought to test if high expression of Drp1(-/17) and the concomitant increase in fused mitochondria may be beneficial to tumor cells when challenged with cisplatin or paclitaxel treatment (Fig. 6a). Expression of Drp1(-/17) led to a statistically significant increase in IC50 values for both compounds in OVCA433 and SKOV3 cells relative to GFP controls (Fig. 6b). Conversely, Drp1(16/17) expression enhanced cell death in response to both compounds compared to GFP control cells, which was particularly evident with Cisplatin (Fig. 6a, b). Notably, cells with Drp1(16/17) expression exhibited the highest caspase 3/7 activity in response to both agents (Fig. 6c), while Drp1(-/17) expression significantly abrogated caspase activity relative to GFP and Drp1(16/17) expressing cells in response to cisplatin and paclitaxel. These data suggest that Drp1(16/17) mediated mitochondrial fission enhances apoptosis of ovarian cancer cells, but that expression of Drp1(-/17), which leads to abrogated mitochondrial fission, protects cells from apoptosis. To determine

if the differences in apoptosis initiation following expression of Drp1 splice variants is due to their differential activation in response to chemotherapeutic agents, phosphorylation of Serine 616 was investigated. Basally, Drp1(-/17) protein displayed less Serine 616 phosphorylation than Drp1(16/17) (Fig. 6d). Although predominantly observed in OVCA433 cells, Drp1(16/17) was more susceptible to phosphorylation at S616 upon treatment with both cisplatin and paclitaxel, while no change in phosphorylation was observed in Drp1(-/17) in response to these agents (Fig. 6e). Taken together, these observations suggest that cells expressing Drp1(-/17) might possess a survival advantage under the selective pressure exerted by chemotherapy, and that this could be partially driven by abrogated phosphorylation in response to pro-apoptotic stimuli.

Endogenous manipulation of Drp1 splice variant expression validates the pro-tumorigenic function of Drp1(-/17).

The data above clearly demonstrate that overexpression of Drp1(-/17), the splice variant lacking exon 16, has significantly different effects on mitochondrial morphology and function, tumor cell behavior and chemosensitivity compared to expression of the full length Drp1(16/17). To rule out that these observations are due to overexpression of recombinant protein, we sought to assess whether altering the endogenous ratios of Drp1 splice variants could elicit similar effects. To achieve this, splice variant-specific siRNAs targeting each of the four endogenous variable domain Drp1/*DNM1L* splice variants were designed (Fig. 7a, b), and used in SKOV3 cells as a model, as this cell line displayed relatively equal expression of all four variable domain Drp1 transcript variants (Fig. 7a), thus allowing us to tune the ratios of their relative expression using siRNAs. Specific knock-down of individual splice variants transcripts (Fig. 7a) led to altered Drp1 protein variant expression (Fig. 7b). While it was more difficult to resolve Drp1(16/17) and Drp1(16/-) on SDS-PAGE due to their close molecular weight individual knockdowns of Drp1 protein variants could be distinctly visualized (Fig. 7b). A positive control siRNA designed to target Exon 15 led to decreased protein expression of all variants (Fig. 7b, lane 2). The knock-down of all variants (siDrp1 total) resulted in fused mitochondrial morphology as expected, and as demonstrated by previous studies targeting Drp1 by RNAi [41-43] (Fig. 7c,d). While knocking down each variant did enhance mitochondrial length and networking to some extent, we observed a varying degree of impact depending on the specific variant targeted (Fig. 7c, d and Extended Data Fig. 9a, b). Drp1(16/17) knockdown most closely replicated the highly elongated mitochondrial morphology and increased branching seen with

total Drp1 knockdown (siDrp1-total, Fig. 7c, d). In contrast, the knockdown of siDrp1(-/17) resulted in less substantial increases in mitochondrial length and networking (Fig. 7c, d), again highlighting that Drp1(-/17) contributes less to mitochondrial fission than Drp1 (16/17). Knockdowns of Drp1(-/16) and siDrp1(-/-) resulted in less elongated mitochondrial morphology compared to siDrp1(16/17), albeit with slight increases compared to siDrp1(-/17) (Extended Data Fig. 9a, b). The combination knockdown of Drp1(-/16) and Drp1(-/-), which essentially enriches for higher but equal expression of Drp1(16/17) and Drp1(-/17), led to an intermediary increase in mitochondrial length and branching (Fig. 7c, d). This suggests that the endogenous ratio of expression between the Drp1(16/17) and Drp1(-/17) variants may be critical in determining the overall fission activity of Drp1. Collectively, these results confirm our overexpression data (Fig. 3), suggesting that the Drp1(16/17) variant plays a more active role in Drp1-mediated mitochondrial fission, while Drp1(-/17) may have a lower capacity to elicit mitochondrial fission.

Importantly, the functional consequences of altered Drp1 splice variants expression on mitochondrial function could similarly be recapitulated using siRNA to target endogenous Drp1 transcripts. We previously showed that Drp1(16/17) overexpression was detrimental to mitochondrial respiratory function while Drp1(-/17) overexpression improved OCR (Fig. 4 and Extended Data Fig. 7). In concurrence, inhibition of Drp1(16/17) improved respiration while siRNA targeting of Drp1(-/17) decreased both basal and ATP-linked oxygen consumption rate (OCR) when compared to siRNA control transfected cells (Fig. 8a, b). No significant changes in mitochondrial function were observed upon combined knockdown of Drp1(16/-) and Drp1(-/-), which maintained equal expression of Drp1(16/17) and Drp1(-/17) (Fig. 8c), again suggesting that an imbalance of their expression may lead to very different mitochondrial morphology and functional consequences.

Subsequently, we investigated the changes in cellular proliferation and migration upon perturbation of endogenous Drp1 variants (Fig. 8d, e, f). Compellingly, increased cellular proliferation was only seen when Drp1(16/17) was knocked down, or when specific enrichment of Drp1(-/17) was achieved by a combined knockdown of the other three variable domain variants (siDrp1(16/17),(-/16) and (-/-); Fig. 8e). These conditions mimic Drp1(-/17) overexpression (Fig. 5b) and mirror the low Drp1(16/17):high Drp1(-/17) expression observed in the TCGA patient cohort that was marked by poor patient outcome (Fig. 2f). All other individual or combination knock-downs of Drp1 transcript variants had little effect on proliferation (Fig. 8e and Extended Data Fig. 9d). Moreover, cell migration was enhanced following single knockdown

of Drp1(16/17), whereas it significantly decreased after single knockdown of Drp1(-/17) variant compared to the control (Fig. 8f). No difference in migration was observed in cells with equal expression of Drp1(-/17) and Drp1(16/17) in following siDrp1(-/16) & Drp1(-/-) knock-down or in cells with single knockdown of either Drp1(16/-) or Drp1(-/-) (Fig. 8f and Extended Data Fig. 9d). Finally, total knockdown of all Drp1 transcripts (siDrp1-total) drastically reduced both cellular proliferation and migration, indicating a differential response to total Drp1 perturbation and variant-specific knockdown. The increased cell proliferation and migration observed with high Drp1(-/17):low Drp1(16/17) expression upon variant-specific knockdown emphasizes the pro-tumorigenic capacity of the Drp1(-/17) variant. These findings echo TCGA data, where poorer patient survival was associated with low Drp1(16/17):high Drp1(-/17) ratios. The above findings also emphasize the importance of the expression ratio between the Drp1(16/17) and Drp1(-/17) variants. This is evidenced by the observation that a combined knockdown of Drp1(-/16) and Drp1(-/-), reflecting an equal expression (50:50) of Drp1(16/17) and Drp1(-/17), led to relatively minor changes in mitochondrial morphology, with no significant impact on mitochondrial function, cellular proliferation, or migration. Taken together, these data validate our previous observations from the overexpression of the Drp1(-/17) and Drp1(16/17) variants, and they emphasize the importance of maintaining a balanced ratio of expression between these two variants for optimal mitochondrial morphology and function as this balance may play a critical role in cancer progression.

Discussion

To our knowledge this is the first description of Drp1/*DNM1L* transcript variants and their functional significance in a pathophysiological setting. While Drp1 has been extensively studied in various diseases, including multiple cancers [12, 14, 44-46], the investigation of different Drp1 isoforms arising from alternate splicing has remained limited, with few studies conducting direct comparisons [26, 27, 29, 32, 47]. Moreover, prior research has often neglected to specify which Drp1 isoform was the subject of study. It is assumed that studies investigating the function of Drp1 in cancer cells utilized plasmid that contains all exons of the variable domain (i.e., Drp1(16/17)) to overexpress recombinant Drp1, or that knock-down strategies targeted the expression of all Drp1 variants. Given our findings that alternate splicing of exon 16 is an important feature of ovarian cancer that is associated with poor patient outcome, and that alternate splicing of exon 16 results in expression of 2 *DNM1L*/Drp1 proteins with distinct function related to regulation of

mitochondrial form and function, future studies focused on Drp1 should take expression and function of *DNM1L*/Drp1 splice variants into consideration.

According to TCGA data the *DNM1L* gene is amplified in >50% serous ovarian cancer cases (5% high level amplification, 46% low level gain), while only 7% of cases show heterozygous loss (Extended Data Fig.2e). Published work has correlated *DNM1L* amplification with enhanced cell cycle gene expression and poor survival in chemo-resistant and recurrent cancer samples [12, 31]. Notably, previous analyses of mRNA expression did not discern levels of specific Drp1 splice variants, leaving it uncertain which transcripts are associated with cell cycle gene expression, prognosis, and chemoresistance. We found that ovarian cancer cells derived from patient ascites, as well as TCGA ovarian cancer specimens predominantly express a transcript lacking exon 16 [Drp1(-/17)]. Strikingly, high Drp1(-/17) expression correlates with poorer overall patient survival. This identification of a specific Drp1 splice variant linked to unfavorable patient outcomes holds crucial clinical implications. It suggests that Drp1(-/17) expression confers advantages to ovarian cancer cells, making the relative expression of Drp1(-/17) versus Drp1(16/17) a predictive marker for outcomes. Moreover, it underscores the clinical impact of Drp1 splice variant expression in ovarian cancer for the first time.

We established that the two major ovarian cancer Drp1 splice variants, Drp1(-/17) and Drp1(16/17) have distinct localization and effects on mitochondrial morphology and function. Drp1(-/17) variant was previously reported to localize to microtubules, and this association shown to consequently result in decreased fission activity compared to Drp1(16/17)[27]. Similarly, we observed that Drp1(-/17) associated more frequently with microtubules, rather than mitochondria compared to Drp1(16/17). This decrease in mitochondrial association likely explains why Drp1(-/17) expression shifts mitochondrial morphology towards a fused state. Importantly, through splice-specific knockdown of Drp1 variants, we provide the first validation of the fusion phenotype associated with Drp1(-/17) at endogenous expression levels. The variant specific knockdowns also emphasize the significance of stoichiometric expression of the Drp1 splice variants in fine tuning regulation of mitochondrial morphology, possibly representing a novel mechanism exploited by cancer cells to manipulate their mitochondrial dynamics and subsequently mitochondrial function.

Decreased fission, and a consequentially more fused mitochondria network has been shown to enhance electron transport chain super-complex assembly and to improve mitochondrial respiratory function[39, 48]. We demonstrated that Drp1(-/17) expression is associated with enhanced mitochondrial respiratory function and more compact cristae arrangement potentially enabling cancer cells to thrive under stress when heightened

mitochondrial function is necessary. Stress-induced mitochondrial hyperfusion has been shown to confer resistance to subsequent insults, promoting cell survival[35, 49, 50]. Similarly, the fused networks resulting from elevated Drp1(-/17) expression likely allow ovarian cancer cells to bolster mitochondria robustness and maintain metabolic efficiency.

Numerous investigations have emphasized the significance of dynamically adapting mitochondrial morphology, as it plays a pivotal role in metabolic flexibility and cell survival in a context-dependent manner [35, 49-53]. Furthermore, the preference for metabolic fuels is closely associated with mitochondrial architecture[53-55]. Indeed, our study not only establishes altered mitochondrial function associated with Drp1 variant expression but also unveils subsequent metabolic reprogramming in these cells, illustrating the connection between mitochondrial morphology and metabolic adaptability driven by these splice variants. The profile of total metabolites in cells expressing Drp1(-/17) underscores a notably active metabolic phenotype, characterized by elevated glycolysis and TCA cycle metabolites. Recent research highlights that cancer cells derive energy not solely from glycolysis but also from mitochondrial respiration [56, 57]. Additionally, ovarian cancer stem cells and chemoresistant cells exhibit a remarkably adaptable metabolic phenotype, capable of switching between glycolysis and oxidative phosphorylation depending on which pathway confers a selective growth advantage and chemoresistance[30, 35, 52, 56, 58-60]. Moreover, metabolic alterations are essential to sustain unbridled growth in cancer cells, with increased ATP synthesis and a shift towards de novo macromolecule biosynthesis. While the increased mitochondrial networking observed in Drp1 (-/17) and cristae architecture potentially contributes to ETC complex assembly and efficiency in oxidative phosphorylation, the observed increase in TCA cycle metabolites suggestive an increase in TCA cycle flux, which could be driven by the need for NADH reducing equivalents, as demonstrated by increased levels of NADH in Drp1 (-/17) cells. It remains to be determined if mitochondrial architecture also contributes to the activity or efficiency of TCA cycle enzymes, although it is known that substrate availability is enhanced by a more fused mitochondrial network [36, 39].

Prior metabolic profiling of ovarian cancer cells and tumors derived from patients has revealed discernible differences in purine and pyrimidine metabolism, glycerolipid metabolism, and energy metabolism [59, 61, 62] Interestingly, akin to earlier observations in ovarian cancer tumors compared to borderline cases, Drp1(-/17) expression correlated with heightened levels of amino acids like glutamine, glycine, and aspartate, all crucial components for purine and pyrimidine metabolism. Furthermore, the decreased serine levels and increased glycine levels associated with Drp1(-/17) expression suggest enhanced catabolism of the nonessential amino acid serine through the mitochondrial one-carbon unit pathway, essential for purine nucleotide

synthesis. This underscores the potential of Drp1(-/17) expression to enable ovarian cancer cells to elevate mitochondrial fidelity, potentially granting greater metabolic flexibility in the face of shifting nutrient availability and conferring survival advantages when subjected to metabolic selection pressures during tumor progression.

Another significant observation is that the diminished fission accompanied by Drp1(-/17) expression leads to enhanced cell survival, proliferation, and increased resistance to apoptosis. This implies a potential advantage for these cells under chemotherapeutic pressures. Drp1 has been extensively studied as a regulator of cell death and proliferation. On one hand, Drp1-mediated fission is crucial for mitosis in cancer cells [14, 15], while on the other hand, fragmented mitochondria hinder the G1-S transition in cells, which is linked to the accumulation of cyclin E and a hyperfused mitochondria [63]. Similarly, elevated mitochondrial fusion has been identified as a feature of ovarian cancer neoplastic stem cells, priming them for self-renewal and proliferation [64]. We predict these conflicting reports related to Drp1 expression and cell proliferation might be partially resolved by considering Drp1 variant expression. Especially as our findings with splice variant specific Drp1 knockdown show distinct impact of Drp1 variants on cell proliferation, with Drp1(-/17) variant primarily associated with enhanced cell survival and proliferation.

Furthermore, since Drp1-mediated mitochondrial fission is essential for initiating apoptosis, the lack of coordinated fission and the resultant fused mitochondria in Drp1(-/17) expressing cells could account for the observed resistance to apoptosis upon exposure to agents like cisplatin and paclitaxel. We propose that this heightened resistance to chemotherapy, coupled with the survival advantages conferred by improved mitochondrial function, contribute to the poorer outcomes observed in patients with high tumor expression of Drp1(-/17). Intriguingly, previous reports on chemoresistant ovarian cancer cells indicate a higher abundance of tubular and elongated mitochondria, potentially suggesting that enhanced fusion could be a mechanism through which tumors evade apoptosis [65, 66]. Given the unique association of Drp1(-/17) with microtubules, the target site of taxanes, further investigations are warranted to ascertain whether the heightened chemoresistance conferred by Drp1(-/17) is attributed to reduced mitochondrial fission or its interaction with microtubules. The interaction of Drp1 with microtubules was previously shown to be driven by direct, electrostatic interactions between the conserved basic residues in Drp1 exon 17 (Arg566/567) and the acidic N-termini of α/β-tubulin. The existence of exon 16 in the Drp1(16/17) sequence is hypothesized to impede this interaction, possibly by physically obscuring or neutralizing the positive charge of the neighboring microtubule binding domain [27]. Future work is needed to elucidate potential extra

mitochondrial function of Drp1(-/17) and how these could be additionally contributing not only to the abrogated fission activity of this protein, but other cellular functions that play a role in driving the enhanced tumorigenic features of cells predominantly expressing this variant.

While our work focused on ovarian cancer, the importance of Drp1 splice variants in other tumor types requires further investigation. Other shortcomings of this work that require further investigation are the lack of understanding as to why and how exon 16 is specifically spliced out in ovarian cancer cells. While cancer cells in general are known for their alterations in RNA splicing and processing [47, 67, 68] it remains to be determined if specific alterations in the RNAs splicing machinery give rise to higher expression of Drp1(-/17). As such, aberrant expression of RNA splice factors such as SRSF3 is associated with ovarian cancer [69, 70].

In summary, our study sheds light on the pathophysiological importance of Drp1 variant expression and their ability to modify mitochondrial fission and fusion dynamics as a novel mechanism underlying ovarian cancer cell plasticity. This study also emphasizes the necessity of expanding our comprehension of these Drp1 splice variants, potentially beyond the scope of cancer, and their consideration in future investigations on the function of Drp1 in different (patho)physiological settings.

Materials & Methods

Cell lines and cell culture

Cell lines were generously provided by the following investigators: OVCA433, OVCA420 Dr. Susan K. Murphy; HeyA8, Dr. Katherine Aird; FT282, Dr. Ronny Drapkin. ES-2, TOV-21-G and OVCAR3 cells were purchased from American Type Culture Collection (ATCC, CRL-1978, HTB-161). OVCA433, OVCA420, SKOV3 and HeyA8 cells were cultured in RPMI 1640 medium (Corning,10-040-CV) supplemented with 10% fetal bovine serum, FBS (Avantor® Seradigm,1500-500). OVCA433 and SKOV3 cells under selection were maintained in fully supplemented growth media with 5ug/ml Puromycin (Gibco™, A1113803). OVCAR3 cells were cultured in RPMI1640 medium supplemented with 0.01 mg/ml bovine insulin (Fisher Scientific,50-608-896) and 10% FBS ES-2 cells were cultured in Modified McCoy's 5a Medium (Corning,10-050-CV) with 10% FBS. TOV-21-G cells were cultured in a 1:1 mix of MCDB 105 (Sigma-Aldrich,117-500) containing 1.5 g/L sodium bicarbonate (Gibco™,25080094) and Medium 199 (Corning,10-060-CV) containing 2.2 g/L sodium bicarbonate, with 15% FBS. FT282 cells were cultured in 50% DMEM and 50% Ham's F-12 medium (Corning,10-090-CV) supplemented with 2% FBS. All cells were maintained at 37°C with 5% CO_2. Cell lines were routinely tested for

Mycoplasma contamination using EZ-PCR™ Mycoplasma Detection Kit (Captivate Bio,20-700-20). Cell line authentication was carried by STR genotyping (Labcorp).

Patient ascites derived EOC cells.

Epithelial Ovarian Cancer (EOC) cells were isolated from malignant ascites of ovarian cancer patients treated at the Women's Cancer Care clinic (Albany, NY) and the Penn State Hershey College of Medicine Division of Gynecologic Oncology, with approval granted from the State University of New York at Albany and the Penn State College of Medicine IRBs. Histological subtype and staging of EOC samples shown in Fig. 2c. Following procurement of ascites EOCs were immediately isolated and cultured as previously described[71], and maintained in culture at 37°C, 5% CO_2 in MCDB/M199 medium supplemented with 10% FBS and penicillin/streptomycin.

Matched tumor specimens

Archival matched specimens of normal fallopian tube or ovary, ovarian tumor and omental tumor from high grade serous ovarian cancer patients were obtained through an honest broker from the ProMark biospecimens bank at the University of Pittsburgh Magee Womens Research Institute, with approval granted from the University of Pittsburgh IRB. Histological subtype and staging of tumor specimens shown in Extended Fig. 3b.

5'/3' Rapid amplification of cDNA ends (RACE)

3' and 5'RACE reactions were carried out using the SMARTer 3'5' RACE kit (Takara), essentially as recommended by the manufacturer. 5'RACE was carried out with the Universal Primer A Mix (UPM) and the *DNM1L* specific antisense primer, positioned in Exon 12: 5' GTTCCACACAGCGGAGGCTGGGC 3'. 3'RACE was carried out using *DNM1L* primer spanning the exon junction of exon 6/7: 5' GATTACGCCAAGCTTTGCCAGGAATGACCAAGGTGCCTGT-3', followed by nested PCR on the PCR product using *DNM1L* specific primers in exon 10/11: 5' GATTACGCCAAGCTTACTTCGGAGCTATGCGGTGGTGCT-3'. RACE PCR products were resolved on a 10% agarose gel, bands gel purified and cloned into the pRACE vector for subsequent sequencing of inserts. Poly A sites were annotated to the *DNM1L* gene using the NCBI genome browser tracks for PolyA sites and clusters, Polyadenylation sits from PolyA_DB (v.3.2) and the polyadenylations sites from the PolyASites at the University of Basel.

Drp1/DNM1L variant RT-PCR

Total RNA from cells and tissue was isolated using Direct-zolTM RNA Miniprep kit (Zymo Research, R2052). Prior to RNA purification tissue was crushed under liquid Nitrogen and 25-50 mg of tissue-powder lysed in 800ml Ambion TRIzol Reagent (Invitrogen™,15596018) overnight at 4°C. First-strand cDNA synthesis was performed using qScript cDNA Synthesis Kit (Quantabio, 95047) according to the manufacturer's instruction. RT-PCR was performed using diluted cDNA (1:5 in water) and PrimeStar DNA Polymerase (Takara, R010A) with primers and PCR conditions listed in Table 1. The amplified products, mixed with Gel Loading Buffer II (Thermo Scientific,AM8547), were separated on a PA-TBE gel and stained with GelStarTM Nucleic Acid Gel Stain (Lonza, 50535).

Primer	Sequence (S: sense; AS: antisense)	PCR Cycle
Drp1 Variable Domain Variants (Exons 16/17)	S: 5'-GGCAATTGAACTGGCTTATATCAACAC-3' AS: 5'-TGGTTGGTTCTTGAACACCATCTCCAA-3'	98C-15s, (98C-10s, 70C-15s, 72C-20s) X32
Drp1 ΔC truncated Variants	S: 5'-GGCAATTGAACTGGCTTATATCAACAC-3' AS: 5'-TAGATA CCACTACACAAACAGGTTCTT-3'	98C-15s, (98C-10s, 70C-15s, 72C-20s) X32-40
Total Drp1 (Exons 1-2)	S: 5'-GTGGGCCCCGGCCCCATTCAT-3' AS: 5'- CAGTACCTCTGGGAAGCAGGTCCCTCC-3'	95C-3m, (95C-10s, 68C-15s, 72C-20s) X32
Actin	S: 5'-AACTGGGACGACATGGAG-3' AS: 5'- TAGCACAGCCTGGATAGCAACGTA-3'	98C-15s, (98C-10s, 70C-15s, 72C-20s) X24

siRNA-mediated knock-down

Cells were transfected with scramble non-targeting SMARTpool control (Dharmacon#D-001810-10-05) or single or combination of Drp1 variant specific siRNA oligonucleotides against target sequence listed in Table 2 using Lipofectamine RNAiMAX (Invitrogen, 13778150). 48 hours post-transfection cells were seeded for experiments. For each experiment, knock-down was confirmed by RT-PCR using Drp1 variable domain variant RT-PCR primers, as above.

Drp1 siRNA	Target Sequence - 5'-3'	Target location
siDrp1(total)	GAGAAACAGGCTAGCCAGAGAATTACCTTCA	Exon 15
siDrp1(16/17)	GAGGCTGATGGCAAGTTAATTCAGGACAGCA	Exon 16/17 junction
siDrp1(-/17)	CTGTATCACGAGACAAGTTAATTCAGGACAG	Exon 15/17 junction
siDrp1(16/-)	GAGGCTGATGGCAAGGTTGCATCTGGAGGTG	Exon 16/18 junction
siDrp1(-/-)	CTGTATCACGAGACAAGGTTGCATCTGGAGG	Exon 15/18 junction

Immunoblotting

Cells were cultured to sub-confluency and lyzed in RIPA buffer (Thermo Scientific™, 89901) containing protease and phosphatase inhibitors (Thermo Scientific™, 78443). The protein supernatant was collected following 30 mins rotation at 4°C, followed by maximum speed (21,000 rcf) centrifugation for 30 mins in a 1.5 ml tabletop centrifuge at 4°C. Protein concentrations were measured using the Pierce BCA protein assay kit (Thermo Scientific™, 23225). Following SDS-PAGE, proteins were transferred to PVDF membranes. Membranes were blocked for an hour in in 5% non-fat milk (Bio-Rad,1706404)/TBS, 0.1% Tween20 (MilliporeSigma, 900-64-5) and were probed overnight at 4°C in primary antibodies. The next day blots were incubated for 1 hour at room temperature with horseradish peroxidase (HRP)-conjugated secondary antibodies and were developed using SuperSignal™ West Femto Maximum Sensitivity Substrate Femto (Thermo Scientific™, 34096).

Antibodies used:

Antibody	Manufacturer	Cat #	Dilution
Drp1	abcam	184247	1:1000
Drp1	EMD Millipore	ABT155	1:1000
Drp1/DLP1	BD Transduction	611112	1:1000
Phospho-DRP1 (Ser616)	Cell Signaling	3455	1:1000
MitoBiogenesis™ Western Blot Cocktail	abcam	123545	1:250
β-actin (9f3)	Thermo Scientific	AM4302	1:1000
β-tubulin (AC-15)	Cell Signaling	2128	1:1000
GAPDH (0411)	Santa Cruz	sc-47724	1:1000
Vinculin	Sigma-Aldrich	Aldrich V9131	1:1000
Amersham ECL HRP conjugated rabbit IgG	Cytiva	NA934	1:10000
Amersham ECL HRP conjugated mouse IgG	Cytiva	NA931	1:10000

TCGA data analysis

RNAseq bam files for the TCGA serous ovarian carcinoma cohort (n = 379, all cases regardless of grade and stage) were downloaded from dbGaP and stored on a secure server according to dbGaP protocols. The samtools 1.9.0 software [72] was used to convert each bam file to two fastq files corresponding to the paired end reads after randomizing the order of the reads with 'samtools collate.' The salmon 1.3.0 software [73] was then applied to quantify genome-wide

transcript abundances based on an index created from a custom reference fasta file, as described below, that incorporates sequences from splice variants and alternate polyadenylation forms of DNML1. The --seqBias, --gcBias, and --validateMapping options for the salmon quant command were utilized. The salmon index was created by following the steps outlined at https://combine-lab.github.io/alevin-tutorial/2019/selective-alignment/. First, a decoys.txt file was created using the GRCh38 primary assembly fasta file. Next, a custom version of the gencode.v22.pc_transcripts.fa file was made by removing all transcripts corresponding to the DNML1 gene and replacing them with sequences corresponding to the alternate splice and alternative polyadenylated transcripts of *DNML1*. Concatenating this custom transcriptome fasta file with the GRCh38 primary assembly fasta file yielded the gentrome fasta file that, along with the decoys.txt file, was used to produce the salmon index. Overall survival data was obtained using cBioportal.

Drp1 plasmids & subcloning

Rat Drp1(-/17) and Drp1(16/17) cloned in pEGFP-C1 plasmids were kindly provided by Dr. Stefan Strack, University of Iowa [27]. Drp1 coding sequence were subcloned into pLenti-CMV-MCS-GFP-SV-puro (Addgene, 73582) with a N-terminal GFP tag and sequenced to confirm successful cloning of Drp1(-/17) and Drp1(16/17) plasmids. The plasmids were transfected in 293-FT cells for expression and lentiviral particle production. OVCA433 and SKOV3 cells were infected and transduced with the GFP vector control, GFP-Drp1(-/17) and GFP-Drp1(16/17) virus, selected for expression using 5ug/ml Puromycin for 1-2 weeks and sorted for GFP expression by flow cytometry to generate stable Drp1 overexpressing cells.

Immunofluorescence and analysis of mitochondrial morphology

Prior to imaging, mitochondria were labelled in cells by transduction with pLV-mitoDsRed virus (Addgene, Plasmid 44386) harvested post expression in 293-FT cells and lentiviral particle production. For imaging, cells were seeded at 60-70% confluency in Chambered Cell Culture slides (Falcon, 08-774-25). Next day, cells were washed once with 1X PBS (Corning, 21-040-CV) and fixed in 4% formaldehyde, made fresh by diluting 16% PFA solution (BTC BeanTown Chemical,30525-89-4) in 1X PBS for 10 mins at room temperature. For imaging FCCP treatment, cells were incubated with 1μM FCCP(Sigma) in media for 30 mins prior to fixation. Post fixation, cells were rinsed twice with 1X PBS and permeabilized for 10-15 mins using 0.2 % Triton™ X-100 (Fisher Scientific, BP151500) in 1X PBS with gentle rocking. Followed by two more PBS rinses prior to 1 hour incubation with SuperBlock™ Blocking Buffer (Thermo

Scientific™,37515) for blocking non-specific antibody binding. Cells were stained with primary antibody against Tubulin (Abcam, ab6160) at 1:1000 dilution in SuperBlock™ blocking buffer for either 1hr 30 mins at room temperature or overnight at 4°C. After incubation cells were washed for three subsequent 10 min washes with 1X PBS with gently rocking. Cells were incubated with 1:1000 dilution of secondary rat antibody conjugated with Alexa Fluor® 647 (abcam, 150167) in SuperBlock™ Blocking Buffer at room temperature for 30 mins. After, washed with 1X PBS for three times,10 mins each to remove any residual antibody. Slides were mounted in ProLong™ Gold Antifade Mountant with DNA Stain DAPI (Invitrogen™, P36935) and dried overnight in dark at room temperature. For mitochondrial imaging of SKOV3 post siRNA transfection, cells were seeded on 35mm glass bottom dishes (MatTek, P35GC-1.5-14-C). Next day cells were stained using MitoTracker™ Green FM (Invitrogen™, M7514) following the manufacturer's recommendations. Briefly, cells were incubated for 12-15 mins in pre-warmed culture medium containing 250 nM MitoTracker™ Green FM and Hoechst 33342 (Thermo Scientific™,62249). After, cells were washed thrice with 1X PBS and imaged in pre-warmed 1X HBSS (Corning, 21-023-CV). Z-stacks were taken with Leica Thunder Imager using 63X oil immersion objective and subjected to inbuilt thunder de-convolution. The mitochondrial network morphology to look at the elongation and fragmentation was performed on 2D Z-stack projections in image J using the mitochondria-analyzer plugin (https://github.com/AhsenChaudhry/Mitochondria-Analyzer). Briefly, the images were converted into binary, and threshold was adjusted to detect the mitochondrial network before performing the 2D per-cell mitochondrial network analysis. Total of at least 150 or more cells were analyzed to get the morphological network parameters with 30 cells or more. analyzed for each biological replicate over at least 3 or more biological replicates. Representative images shown were adjusted in brightness and contrast for better visualization.

TEM

Cells were fixed in cold 2.5% glutaraldehyde (25% glutaraldehyde stock EM grade, Polysciences, 111-30-8) in 0.01 M PBS (Fisher), pH 7.3. Samples were rinsed in PBS, post-fixed in 1% osmium tetroxide (Electron Microscopy Sciences) with 1% potassium ferricyanide, (Fisher), rinsed in PBS, dehydrated through a graded series of ethanol, and embedded in Poly/Bed® 812 (Luft formulations). Semi-thin (300 nm) sections were cut on a Reichart Ultracut (Leica Microsystems), stained with 0.5% Toluidine Blue O (Fisher) in 1% sodium borate (Fisher) and examined under the light microscope. Ultrathin sections (65 nm) were stained with 2% uranyl acetate (Electron Microscopy Science) and Reynold's lead citrate (Lead Nitrate, Sodium Citrate and Sodium Hydroxide, Fisher) and examined on JEOL 1400 Plus transmission electron

673 microscope with a side mount AMT 2k digital camera (Advanced Microscopy Techniques). For
674 morphometric analysis of mitochondria by transmission electron microscopy, mitochondrial
675 area, mitochondrial length (major axis), cristae number and cristae volume density per
676 mitochondria was quantified and analyzed as described[74] using ImageJ. At least 40-50
677 mitochondria per biological replicate over 3 experimental replicates were analyzed.

678 *TMRE Protocol*
679 OVCA433 and SKOV3 were seeded into 96-well plates at a density of 1,000 cells per well and
680 incubated overnight in a cell culture incubator at 37ºC and 5% CO_2. The following day, half the
681 sample wells were treated with 10 µM FCCP and incubated for 30 minutes in a cell culture
682 incubator. All the sample wells were then treated with 100 nM TMRE (Thermo Fisher Scientific,
683 T669), and incubated for 30 minutes at 37ºC in a cell culture incubator. All samples were
684 subsequently washed twice with 1X PBS, and fluorescence measurements were taken with a
685 Synergy HT microplate reader (BioTek) with an excitation wavelength of 530 nm and emission
686 wavelength of 590 nm.
687
688 *MitoSox mitochondrial superoxide indicator*
689 500,000 cells were stained with 5 µM MitoSOX Red mitochondrial superoxide indicator
690 (Invitrogen, M36008) in 1 ml HBSS (Corning, 21-023-CV) for 30 minutes at 37ºC. Following
691 incubation, cells were washed with HBSS, and florescence was measured using flow cytometry
692 as per manufacture's protocol. Unstained cells were used as a negative control while cells
693 treated with 50 µM Antimycin A were used as a positive control for flow cytometry.
694
695 *Bioenergetic Analysis of Oxygen Consumption Rate (OCR) and Extracellular Acidification Rate*
696 *(ECAR)*
697 The Agilent Seahorse XFp Metabolic Analyzer (Agilent, model S7802A) was used to assess
698 mitochondrial respiration of OVCA433 and SKOV3 as described previously for attached cells[75].
699 Briefly, prior to the start of the experiment, cells were evenly seeded and cultured overnight in a
700 Seahorse XFp cell culture plate (Agilent, 103022-100) at a density of 10,000 and 8,000
701 cells/well for OVCA433 and SKOV3, respectively. The XFp sensor cartridge was hydrated in
702 Agilent Seahorse XF Calibrant (Agilent,103022-100) at 37°C in a humidified incubator (non-
703 CO_2) incubator overnight. On the day of the experiment, cell culture media was replaced with
704 pre-warmed seahorse XF base RPMI media, pH 7.4 (Agilent,103576-100) supplemented with 1
705 mM sodium pyruvate (Agilent 103578-100), 2 mM glutamine (Agilent 103579-100), and 10 mM
706 glucose (Agilent, 103577-100). Cells were then placed into a non-CO_2 humidified incubator at

37°C for 60 min. Mitochondrial stress test reagents (pharmacological manipulators of mitochondrial respiratory chain proteins) were diluted in pre-warmed XF assay media to achieve the following final concentrations in the cell culture well: 1.5 μM Oligomycin A (Sigma, 75351); 1 or 0.5 μM FCCP (Sigma, C2920) for OVCA433 and SKOV3, respectively; and 0.5 μM Antimycin A/Rotenone (Sigma, A8674,45656). Three basal rate measurements (3 min measurement time each) were taken prior to the injection of mitochondrial stress test reagents and three measurements of OCR/ECAR were obtained respectively following injection of compounds. Post-run, the cells were stained with crystal violet dye (0.05%) (Sigma-Aldrich, 229288) for seeding normalization. The dye was released from cells using 30% acetic acid and absorbance was measured at 590 nm, using GloMax Explorer (Promega) microplate reader.

Metabolomics

1-2 million cells were seeded in 60 mm dishes per replicate (n=6 for each condition) in normal cell growth media. Next day, cells were washed once with 1X PBS and fresh media was added. After 24 hours, metabolic quenching and polar metabolite pool extraction was performed by adding ice cold 80% methanol (aqueous with 0.1% formic acid) at a ratio of 500µL buffer per 1e6 cells. Deuterated (D3)-creatinine and (D3)-alanine, (D4)-taurine and (D3)-lactate (Sigma-Aldrich) was added to the sample lysates as an internal standard for a final concentration of 10µM. Samples are scraped into Eppendorf tubes on ice, homogenized using a 25°C water bath sonicator and the supernatant was then cleared of protein by centrifugation at 16,000xg. 2µL of cleared supernatant was subjected to online LC-MS analysis. Analyses were performed by untargeted LC-HRMS. Briefly, Samples were injected via a Thermo Vanquish UHPLC and separated over a reversed phase Thermo HyperCarb porous graphite column (2.1×100mm, 3µm particle size) maintained at 55°C. For the 20 minute LC gradient, the mobile phase consisted of the following: solvent A (water / 0.1% FA) and solvent B (ACN / 0.1% FA). The gradient was the following: 0-1min 1% B, increase to 15%B over 5 minutes, continue increasing to 98%B over 5 minutes, hold at 98%B for five minutes, reequillibrate at 1%B for five minutes. The Thermo IDX tribrid mass spectrometer was operated in both positive and ion mode, scanning in ddMS2 mode (2 µscans) from 70 to 800 m/z at 120,000 resolution with an AGC target of 2e5 for full scan, 2e4 for ms2 scans using HCD fragmentation at stepped 15,35,50 collision energies. Source ionization setting was 3.0 and 2.4kV spray voltage respectively for positive and negative mode. Source gas parameters were 35 sheath gas, 12 auxiliary gas at 320°C, and 8 sweep gas. Calibration was performed prior to analysis using the PierceTM

FlexMix Ion Calibration Solutions (Thermo Fisher Scientific). Integrated peak areas were then extracted manually using Quan Browser (Thermo Fisher Xcalibur ver. 2.7).

NAD^+ and NADH level determination

OVCA433 and SKOV3 cells were seeded into flat-bottom 96-well plates at a density of 10,000 and 8,000 respectively in normal growth medium. After overnight incubation, total NAD+ and NADH levels and their ratios were determined using NAD+/NADH-glo assay kit (Promega, G9071) as per manufacture's protocol. Following addition of NAD/NADH-GloTM Detection Reagent, samples were incubated for 1 hour at room temperature and transferred to white flat-bottom 96-well plate (BrandTech® ,BRA-781605). Bioluminescence was measured with GloMax Explorer (Promega) plate reader. Protein Concertation was determined by BCA and used for data normalization.

Cell proliferation and viability

Equal number of cells were seeded into 96 well plates at density of 1000 and 500 cells/well for OVCA433 and SKOV3 respectively, in normal culture medium. For cell proliferation rate, cell numbers were analyzed for 3 days successively using FluoReporter™ Blue Fluorometric dsDNA Quantitation Kit (Invitrogen™, F2962) as per manufacturer's protocol and fluorescence measurements were taken with a Victor X (PerkinElmer) microplate reader with an excitation wavelength of 360 nm and emission wavelength of 460 nm respectively. Proliferation rate was measured as the increase in the cell density relative to day 1. For cell viability in response to chemotherapeutic agents, cells were treated with indicated doses of Cisplatin (cis-Diamineplatinum(II) dichloride) (Sigma) or Paclitaxel(Sigma). Following 72 hours of drug treatment cell viability was measured using FluoReporter™ Blue Fluorometric dsDNA Quantitation Kit and was expressed as percentage survival relative to non-treated cells.

Caspase 3/7 activity assay

OVCA433 and SKOV3 cells were seeded into flat-bottom 96-well plates at a density of 7,000 and 5,000 cells per well respectively in normal growth medium. After overnight incubation, cells were treated with 5 μM Cisplatin (cis-Diamineplatinum(II) dichloride) (Sigma) or 1 nM Paclitaxel(Sigma) respectively. After 24 hours drug treatment, caspase 3/7 activity was measured using Caspase-Glo® 3/7 Assay System- (Promega, G8091) per manufacture's protocol. Briefly, equal volume of reagent was added to the samples and only media control. Following 1 hour incubation in dark at room temperature, samples were transferred to white flat-

bottom 96-well plate (BrandTech® ,BRA-781605) and bioluminescence was measured with GloMax Explorer (Promega) plate reader.

Clonogenicity assay

100 cells/well were seeded in a 6 well plate for single cell survival clonogenicity assay and cultured for 7-10 days under normal culture conditions. Clonogenicity was assessed by staining colonies with crystal violet (0.05%). Colonies were counted using Image J and data expressed as cellular survival fraction.

Migration Assay

For assessment of Transwell migration, cell culture inserts (Corning, 353097) with 8.0 µm Transparent PET Membrane, were each placed into a 24- well plate with 800 µL complete growth medium (with serum) added at the bottom of each well. 50,000 and 30,000 cells of OVCA433 and SKOV3, respectively were seeded onto the top of the Transwell membrane of the insert in 150 µL serum free media. After 24 hours, the Transwelll inserts were removed and washed twice with 1XPBS. The Transwell membrane was fixed and stained with Crystal violet (0.05%) for an hour. The inserts were washed three times with 1X PBS and the non-migrated cells were removed from the top of the membrane using dry cotton swabs. The inserts were dried overnight, and images were taken of the migrated cells at the bottom of the membrane using Leica Thunder Imager with colored K3C camera. The dye was released from cell inserts using 30% acetic acid and absorbance was measured using GloMax Explorer (Promega) microplate reader at 590 nm as a readout for cell migration.

Data and Statistical Analysis

All data presented are from at least three biological replicates and represented as mean ± standard error of the mean. Unless otherwise indicated, statistical data analysis was carried out using GraphPad Prism Software (10.0.2), with appropriate analyses chosen based on experimental design, as stated in figure legends.

Acknowledgements

The authors would like to thank Dr. Stefan Strack for providing Drp1 splice variant plasmids. We would like to thank the following individuals for helpful scientific discussions: Yisang Yoon, Janine Santos, Patrick Kimes. We thank Royden Clark, Emmy Dier, Sara Shimko and Ben Yankasky for technical assistance. This work was supported by the U.S. Department of Defense

CDMRP pilot award W81XWH-16-1-0117, TEAL award W81XWH-22-10252 and NIH R01CA242021 (to N.H.), R01CA230628 (to K.M. & N.H), NIH training grant 2T32HL110849-11A1 (to S.W.), R35-HL150778 (to M.T.), NIHS10OD023402 (to S.L.G.) and NIH instrumentation grants S10RR025488, S10RR016236, S10RR019003 (to S.C.W.). Lauren Borho and Dr. Francesmary Mudugno kindly assisted as honest brokers to access patient specimens. The ProMark tissue bank is supported by NIH SPORE P50CA272218.

Author contributions

Z.J. contributed to conceptual and experimental design, carried out experiments and data analysis, prepared figures and wrote the manuscript. D.H.S contributed to experimental design, carried out experiments and data analysis. W.P., S.W., A.E., S.K., Y.-Y.C., J.C.B., A.E.A., M.S., S.J.M., carried out experiments and performed data analysis. R.P., H.G.W., S.Y., S.C.W., S.G.W., N.L., L.C., K.A. contributed to conceptual ideas and manuscript editing. M.T., V.W., and K.M. contributed to conceptual and experimental design, data analysis and interpretation, and manuscript editing. N.H. supervised and conceived the study, contributed to conceptual and experimental design, assisted in data analysis, writing and editing of the manuscript.

Conflict of interest

The authors have no conflicts of interest.

References

1. Kamerkar SC, Kraus F, Sharpe AJ, Pucadyil TJ, Ryan MT. Dynamin-related protein 1 has membrane constricting and severing abilities sufficient for mitochondrial and peroxisomal fission. Nat Commun. 2018;9(1):5239. Epub 2018/12/12. doi: 10.1038/s41467-018-07543-w. PubMed PMID: 30531964; PMCID: PMC6286342.

2. Archer SL. Mitochondrial dynamics--mitochondrial fission and fusion in human diseases. N Engl J Med. 2013;369(23):2236-51. Epub 2013/12/07. doi: 10.1056/NEJMra1215233. PubMed PMID: 24304053.

3. Santel A, Frank S. Shaping mitochondria: The complex posttranslational regulation of the mitochondrial fission protein DRP1. IUBMB Life. 2008;60(7):448-55. Epub 2008/05/10. doi: 10.1002/iub.71. PubMed PMID: 18465792.

4. Yu R, Jin SB, Ankarcrona M, Lendahl U, Nister M, Zhao J. The Molecular Assembly State of Drp1 Controls its Association With the Mitochondrial Recruitment Receptors Mff and

MIEF1/2. Front Cell Dev Biol. 2021;9:706687. Epub 2021/11/23. doi: 10.3389/fcell.2021.706687. PubMed PMID: 34805137; PMCID: PMC8602864.

5. Yamada T, Adachi Y, Iijima M, Sesaki H. Making a Division Apparatus on Mitochondria. Trends Biochem Sci. 2016;41(3):209-10. Epub 2016/02/18. doi: 10.1016/j.tibs.2016.02.001. PubMed PMID: 26879678; PMCID: PMC5378552.

6. Cribbs JT, Strack S. Reversible phosphorylation of Drp1 by cyclic AMP-dependent protein kinase and calcineurin regulates mitochondrial fission and cell death. EMBO Rep. 2007;8(10):939-44. Epub 2007/08/28. doi: 10.1038/sj.embor.7401062. PubMed PMID: 17721437; PMCID: PMC2002551.

7. Strack S, Cribbs JT. Allosteric modulation of Drp1 mechanoenzyme assembly and mitochondrial fission by the variable domain. J Biol Chem. 2012;287(14):10990-1001. Epub 2012/02/16. doi: 10.1074/jbc.M112.342105. PubMed PMID: 22334657; PMCID: PMC3322891.

8. Parone PA, Da Cruz S, Tondera D, Mattenberger Y, James DI, Maechler P, Barja F, Martinou JC. Preventing mitochondrial fission impairs mitochondrial function and leads to loss of mitochondrial DNA. PLoS One. 2008;3(9):e3257. Epub 2008/09/23. doi: 10.1371/journal.pone.0003257. PubMed PMID: 18806874; PMCID: PMC2532749.

9. Benard G, Bellance N, James D, Parrone P, Fernandez H, Letellier T, Rossignol R. Mitochondrial bioenergetics and structural network organization. J Cell Sci. 2007;120(Pt 5):838-48. Epub 2007/02/15. doi: 10.1242/jcs.03381. PubMed PMID: 17298981.

10. Twig G, Elorza A, Molina AJ, Mohamed H, Wikstrom JD, Walzer G, Stiles L, Haigh SE, Katz S, Las G, Alroy J, Wu M, Py BF, Yuan J, Deeney JT, Corkey BE, Shirihai OS. Fission and selective fusion govern mitochondrial segregation and elimination by autophagy. EMBO J. 2008;27(2):433-46. Epub 2008/01/18. doi: 10.1038/sj.emboj.7601963. PubMed PMID: 18200046; PMCID: PMC2234339.

11. Arnoult D, Rismanchi N, Grodet A, Roberts RG, Seeburg DP, Estaquier J, Sheng M, Blackstone C. Bax/Bak-dependent release of DDP/TIMM8a promotes Drp1-mediated mitochondrial fission and mitoptosis during programmed cell death. Curr Biol. 2005;15(23):2112-8. Epub 2005/12/08. doi: 10.1016/j.cub.2005.10.041. PubMed PMID: 16332536.

12. Tanwar DK, Parker DJ, Gupta P, Spurlock B, Alvarez RD, Basu MK, Mitra K. Crosstalk between the mitochondrial fission protein, Drp1, and the cell cycle is identified across various cancer types and can impact survival of epithelial ovarian cancer patients. Oncotarget. 2016;7(37):60021-37. Epub 2016/08/11. doi: 10.18632/oncotarget.11047. PubMed PMID: 27509055; PMCID: PMC5312366.

13. Serasinghe MN, Wieder SY, Renault TT, Elkholi R, Asciolla JJ, Yao JL, Jabado O, Hoehn K, Kageyama Y, Sesaki H, Chipuk JE. Mitochondrial division is requisite to RAS-induced transformation and targeted by oncogenic MAPK pathway inhibitors. Mol Cell. 2015;57(3):521-36. doi: 10.1016/j.molcel.2015.01.003. PubMed PMID: 25658204; PMCID: PMC4320323.

14. Kashatus JA, Nascimento A, Myers LJ, Sher A, Byrne FL, Hoehn KL, Counter CM, Kashatus DF. Erk2 phosphorylation of Drp1 promotes mitochondrial fission and MAPK-driven tumor growth. Mol Cell. 2015;57(3):537-51. Epub 2015/02/07. doi: 10.1016/j.molcel.2015.01.002. PubMed PMID: 25658205; PMCID: PMC4393013.

15. Taguchi N, Ishihara N, Jofuku A, Oka T, Mihara K. Mitotic phosphorylation of dynamin-related GTPase Drp1 participates in mitochondrial fission. The Journal of biological chemistry. 2007;282(15):11521-9. Epub 2007/02/16. doi: 10.1074/jbc.M607279200. PubMed PMID: 17301055.

16. Rehman J, Zhang HJ, Toth PT, Zhang Y, Marsboom G, Hong Z, Salgia R, Husain AN, Wietholt C, Archer SL. Inhibition of mitochondrial fission prevents cell cycle progression in lung cancer. FASEB journal : official publication of the Federation of American Societies for Experimental Biology. 2012;26(5):2175-86. Epub 2012/02/11. doi: 10.1096/fj.11-196543. PubMed PMID: 22321727; PMCID: 3336787.

17. Desai SP, Bhatia SN, Toner M, Irimia D. Mitochondrial localization and the persistent migration of epithelial cancer cells. Biophys J. 2013;104(9):2077-88. doi: 10.1016/j.bpj.2013.03.025. PubMed PMID: 23663851; PMCID: PMC3647149.

18. Wieder SY, Serasinghe MN, Sung JC, Choi DC, Birge MB, Yao JL, Bernstein E, Celebi JT, Chipuk JE. Activation of the Mitochondrial Fragmentation Protein DRP1 Correlates with BRAF(V600E) Melanoma. J Invest Dermatol. 2015;135(10):2544-7. doi: 10.1038/jid.2015.196. PubMed PMID: 26032958; PMCID: PMC4567922.

19. Frank S, Gaume B, Bergmann-Leitner ES, Leitner WW, Robert EG, Catez F, Smith CL, Youle RJ. The role of dynamin-related protein 1, a mediator of mitochondrial fission, in apoptosis. Dev Cell. 2001;1(4):515-25. Epub 2001/11/13. PubMed PMID: 11703942.

20. Thomas KJ, Jacobson MR. Defects in mitochondrial fission protein dynamin-related protein 1 are linked to apoptotic resistance and autophagy in a lung cancer model. PloS one. 2012;7(9):e45319. Epub 2012/10/03. doi: 10.1371/journal.pone.0045319. PubMed PMID: 23028930; PMCID: 3447926.

21. Caino MC, Ghosh JC, Chae YC, Vaira V, Rivadeneira DB, Faversani A, Rampini P, Kossenkov AV, Aird KM, Zhang R, Webster MR, Weeraratna AT, Bosari S, Languino LR, Altieri DC. PI3K therapy reprograms mitochondrial trafficking to fuel tumor cell invasion. Proc Natl

907 Acad Sci U S A. 2015;112(28):8638-43. doi: 10.1073/pnas.1500722112. PubMed PMID:
908 26124089; PMCID: PMC4507184.
909 22. Farrand L, Kim JY, Im-Aram A, Suh JY, Lee HJ, Tsang BK. An improved quantitative
910 approach for the assessment of mitochondrial fragmentation in chemoresistant ovarian cancer
911 cells. PLoS One. 2013;8(9):e74008. Epub 2013/09/09. doi: 10.1371/journal.pone.0074008.
912 PubMed PMID: 24040144; PMCID: PMC3767598.
913 23. Kong B, Wang Q, Fung E, Xue K, Tsang BK. p53 is required for cisplatin-induced
914 processing of the mitochondrial fusion protein L-Opa1 that is mediated by the mitochondrial
915 metallopeptidase Oma1 in gynecologic cancers. The Journal of biological chemistry.
916 2014;289(39):27134-45. doi: 10.1074/jbc.M114.594812. PubMed PMID: 25112877; PMCID:
917 PMC4175349.
918 24. Macdonald PJ, Francy CA, Stepanyants N, Lehman L, Baglio A, Mears JA, Qi X,
919 Ramachandran R. Distinct Splice Variants of Dynamin-related Protein 1 Differentially Utilize
920 Mitochondrial Fission Factor as an Effector of Cooperative GTPase Activity. J Biol Chem.
921 2016;291(1):493-507. Epub 2015/11/19. doi: 10.1074/jbc.M115.680181. PubMed PMID:
922 26578513; PMCID: PMC4697187.
923 25. Rosdah AA, Smiles WJ, Oakhill JS, Scott JW, Langendorf CG, Delbridge LMD, Holien
924 JK, Lim SY. New perspectives on the role of Drp1 isoforms in regulating mitochondrial
925 pathophysiology. Pharmacol Ther. 2020;213:107594. Epub 2020/06/01. doi:
926 10.1016/j.pharmthera.2020.107594. PubMed PMID: 32473962.
927 26. Itoh K, Adachi Y, Yamada T, Suzuki TL, Otomo T, McBride HM, Yoshimori T, Iijima M,
928 Sesaki H. A brain-enriched Drp1 isoform associates with lysosomes, late endosomes, and the
929 plasma membrane. J Biol Chem. 2018;293(30):11809-22. Epub 2018/06/02. doi:
930 10.1074/jbc.RA117.001253. PubMed PMID: 29853636; PMCID: PMC6066318.
931 27. Strack S, Wilson TJ, Cribbs JT. Cyclin-dependent kinases regulate splice-specific
932 targeting of dynamin-related protein 1 to microtubules. J Cell Biol. 2013;201(7):1037-51. doi:
933 10.1083/jcb.201210045. PubMed PMID: 23798729; PMCID: PMC3691453.
934 28. Howng SL, Sy WD, Cheng TS, Lieu AS, Wang C, Tzou WS, Cho CL, Hong YR.
935 Genomic organization, alternative splicing, and promoter analysis of human dynamin-like
936 protein gene. Biochem Biophys Res Commun. 2004;314(3):766-72. Epub 2004/01/27. doi:
937 10.1016/j.bbrc.2003.12.172. PubMed PMID: 14741701.
938 29. Chen CH, Howng SL, Hwang SL, Chou CK, Liao CH, Hong YR. Differential expression
939 of four human dynamin-like protein variants in brain tumors. DNA Cell Biol. 2000;19(3):189-94.
940 Epub 2000/04/05. doi: 10.1089/104454900314573. PubMed PMID: 10749171.

30. Dier U, Shin DH, Hemachandra LP, Uusitalo LM, Hempel N. Bioenergetic analysis of ovarian cancer cell lines: profiling of histological subtypes and identification of a mitochondria-defective cell line. PLoS One. 2014;9(5):e98479. Epub 2014/05/27. doi: 10.1371/journal.pone.0098479. PubMed PMID: 24858344; PMCID: PMC4032324.

31. Tsuyoshi H, Orisaka M, Fujita Y, Asare-Werehene M, Tsang BK, Yoshida Y. Prognostic impact of Dynamin related protein 1 (Drp1) in epithelial ovarian cancer. BMC Cancer. 2020;20(1):467. Epub 2020/05/26. doi: 10.1186/s12885-020-06965-4. PubMed PMID: 32448194; PMCID: PMC7247242.

32. Uo T, Dworzak J, Kinoshita C, Inman DM, Kinoshita Y, Horner PJ, Morrison RS. Drp1 levels constitutively regulate mitochondrial dynamics and cell survival in cortical neurons. Exp Neurol. 2009;218(2):274-85. Epub 2009/05/19. doi: 10.1016/j.expneurol.2009.05.010. PubMed PMID: 19445933; PMCID: PMC2733949.

33. Yoon Y, Pitts KR, Dahan S, McNiven MA. A novel dynamin-like protein associates with cytoplasmic vesicles and tubules of the endoplasmic reticulum in mammalian cells. J Cell Biol. 1998;140(4):779-93. doi: 10.1083/jcb.140.4.779. PubMed PMID: 9472031; PMCID: PMC2141745.

34. Michalska BM, Kwapiszewska K, Szczepanowska J, Kalwarczyk T, Patalas-Krawczyk P, Szczepanski K, Holyst R, Duszynski J, Szymanski J. Insight into the fission mechanism by quantitative characterization of Drp1 protein distribution in the living cell. Sci Rep. 2018;8(1):8122. Epub 2018/05/29. doi: 10.1038/s41598-018-26578-z. PubMed PMID: 29802333; PMCID: PMC5970238.

35. Li J, Huang Q, Long X, Guo X, Sun X, Jin X, Li Z, Ren T, Yuan P, Huang X, Zhang H, Xing J. Mitochondrial elongation-mediated glucose metabolism reprogramming is essential for tumour cell survival during energy stress. Oncogene. 2017;36(34):4901-12. Epub 2017/04/25. doi: 10.1038/onc.2017.98. PubMed PMID: 28436948.

36. Skulachev VP. Mitochondrial filaments and clusters as intracellular power-transmitting cables. Trends Biochem Sci. 2001;26(1):23-9. Epub 2001/02/13. doi: 10.1016/s0968-0004(00)01735-7. PubMed PMID: 11165513.

37. Varanita T, Soriano ME, Romanello V, Zaglia T, Quintana-Cabrera R, Semenzato M, Menabo R, Costa V, Civiletto G, Pesce P, Viscomi C, Zeviani M, Di Lisa F, Mongillo M, Sandri M, Scorrano L. The OPA1-dependent mitochondrial cristae remodeling pathway controls atrophic, apoptotic, and ischemic tissue damage. Cell Metab. 2015;21(6):834-44. Epub 2015/06/04. doi: 10.1016/j.cmet.2015.05.007. PubMed PMID: 26039448; PMCID: PMC4457892.

975 38. Cogliati S, Frezza C, Soriano ME, Varanita T, Quintana-Cabrera R, Corrado M, Cipolat
976 S, Costa V, Casarin A, Gomes LC, Perales-Clemente E, Salviati L, Fernandez-Silva P, Enriquez
977 JA, Scorrano L. Mitochondrial cristae shape determines respiratory chain supercomplexes
978 assembly and respiratory efficiency. Cell. 2013;155(1):160-71. Epub 2013/09/24. doi:
979 10.1016/j.cell.2013.08.032. PubMed PMID: 24055366; PMCID: PMC3790458.
980 39. Cogliati S, Enriquez JA, Scorrano L. Mitochondrial Cristae: Where Beauty Meets
981 Functionality. Trends Biochem Sci. 2016;41(3):261-73. Epub 2016/02/10. doi:
982 10.1016/j.tibs.2016.01.001. PubMed PMID: 26857402.
983 40. Karbowski M, Lee YJ, Gaume B, Jeong SY, Frank S, Nechushtan A, Santel A, Fuller M,
984 Smith CL, Youle RJ. Spatial and temporal association of Bax with mitochondrial fission sites,
985 Drp1, and Mfn2 during apoptosis. J Cell Biol. 2002;159(6):931-8. Epub 2002/12/25. doi:
986 10.1083/jcb.200209124. PubMed PMID: 12499352; PMCID: PMC2173996.
987 41. Fonseca TB, Sanchez-Guerrero A, Milosevic I, Raimundo N. Mitochondrial fission
988 requires DRP1 but not dynamins. Nature. 2019;570(7761):E34-E42. Epub 2019/06/21. doi:
989 10.1038/s41586-019-1296-y. PubMed PMID: 31217603.
990 42. Otera H, Wang C, Cleland MM, Setoguchi K, Yokota S, Youle RJ, Mihara K. Mff is an
991 essential factor for mitochondrial recruitment of Drp1 during mitochondrial fission in mammalian
992 cells. J Cell Biol. 2010;191(6):1141-58. Epub 2010/12/15. doi: 10.1083/jcb.201007152. PubMed
993 PMID: 21149567; PMCID: PMC3002033.
994 43. Mopert K, Hajek P, Frank S, Chen C, Kaufmann J, Santel A. Loss of Drp1 function alters
995 OPA1 processing and changes mitochondrial membrane organization. Exp Cell Res.
996 2009;315(13):2165-80. Epub 2009/05/05. doi: 10.1016/j.yexcr.2009.04.016. PubMed PMID:
997 19409380.
998 44. Lima AR, Santos L, Correia M, Soares P, Sobrinho-Simoes M, Melo M, Maximo V.
999 Dynamin-Related Protein 1 at the Crossroads of Cancer. Genes (Basel). 2018;9(2). Epub
1000 2018/02/22. doi: 10.3390/genes9020115. PubMed PMID: 29466320; PMCID: PMC5852611.
1001 45. Banerjee R, Mukherjee A, Nagotu S. Mitochondrial dynamics and its impact on human
1002 health and diseases: inside the DRP1 blackbox. J Mol Med (Berl). 2022;100(1):1-21. Epub
1003 2021/10/18. doi: 10.1007/s00109-021-02150-7. PubMed PMID: 34657190.
1004 46. Xie Q, Wu Q, Horbinski CM, Flavahan WA, Yang K, Zhou W, Dombrowski SM, Huang Z,
1005 Fang X, Shi Y, Ferguson AN, Kashatus DF, Bao S, Rich JN. Mitochondrial control by DRP1 in
1006 brain tumor initiating cells. Nat Neurosci. 2015;18(4):501-10. Epub 2015/03/03. doi:
1007 10.1038/nn.3960. PubMed PMID: 25730670; PMCID: PMC4376639.

1008 47. Ciesla M, Ngoc PCT, Cordero E, Martinez AS, Morsing M, Muthukumar S, Beneventi G,
1009 Madej M, Munita R, Jonsson T, Lovgren K, Ebbesson A, Nodin B, Hedenfalk I, Jirstrom K,
1010 Vallon-Christersson J, Honeth G, Staaf J, Incarnato D, Pietras K, Bosch A, Bellodi C. Oncogenic
1011 translation directs spliceosome dynamics revealing an integral role for SF3A3 in breast cancer.
1012 Mol Cell. 2021;81(7):1453-68 e12. Epub 2021/03/05. doi: 10.1016/j.molcel.2021.01.034.
1013 PubMed PMID: 33662273.
1014 48. Gao T, Zhang X, Zhao J, Zhou F, Wang Y, Zhao Z, Xing J, Chen B, Li J, Liu S. SIK2
1015 promotes reprogramming of glucose metabolism through PI3K/AKT/HIF-1alpha pathway and
1016 Drp1-mediated mitochondrial fission in ovarian cancer. Cancer Lett. 2020;469:89-101. Epub
1017 2019/10/23. doi: 10.1016/j.canlet.2019.10.029. PubMed PMID: 31639424.
1018 49. van der Bliek AM. Fussy mitochondria fuse in response to stress. EMBO J.
1019 2009;28(11):1533-4. Epub 2009/06/06. doi: 10.1038/emboj.2009.130. PubMed PMID:
1020 19494844; PMCID: PMC2693156.
1021 50. Tondera D, Grandemange S, Jourdain A, Karbowski M, Mattenberger Y, Herzig S, Da
1022 Cruz S, Clerc P, Raschke I, Merkwirth C, Ehses S, Krause F, Chan DC, Alexander C, Bauer C,
1023 Youle R, Langer T, Martinou JC. SLP-2 is required for stress-induced mitochondrial hyperfusion.
1024 EMBO J. 2009;28(11):1589-600. Epub 2009/04/11. doi: 10.1038/emboj.2009.89. PubMed
1025 PMID: 19360003; PMCID: PMC2693158.
1026 51. Grieco JP, Allen ME, Perry JB, Wang Y, Song Y, Rohani A, Compton SLE, Smyth JW,
1027 Swami NS, Brown DA, Schmelz EM. Progression-Mediated Changes in Mitochondrial
1028 Morphology Promotes Adaptation to Hypoxic Peritoneal Conditions in Serous Ovarian Cancer.
1029 Front Oncol. 2020;10:600113. Epub 2021/02/02. doi: 10.3389/fonc.2020.600113. PubMed
1030 PMID: 33520711; PMCID: PMC7838066.
1031 52. Anderson AS, Roberts PC, Frisard MI, Hulver MW, Schmelz EM. Ovarian tumor-initiating
1032 cells display a flexible metabolism. Exp Cell Res. 2014;328(1):44-57. Epub 2014/08/31. doi:
1033 10.1016/j.yexcr.2014.08.028. PubMed PMID: 25172556; PMCID: PMC4260041.
1034 53. Ngo J, Choi DW, Stanley IA, Stiles L, Molina AJA, Chen PH, Lako A, Sung ICH,
1035 Goswami R, Kim MY, Miller N, Baghdasarian S, Kim-Vasquez D, Jones AE, Roach B, Gutierrez
1036 V, Erion K, Divakaruni AS, Liesa M, Danial NN, Shirihai OS. Mitochondrial morphology controls
1037 fatty acid utilization by changing CPT1 sensitivity to malonyl-CoA. EMBO J.
1038 2023;42(11):e111901. Epub 2023/03/15. doi: 10.15252/embj.2022111901. PubMed PMID:
1039 36917141; PMCID: PMC10233380.

54. Alan L, Scorrano L. Shaping fuel utilization by mitochondria. Curr Biol. 2022;32(12):R618-R23. Epub 2022/06/22. doi: 10.1016/j.cub.2022.05.006. PubMed PMID: 35728541.

55. Liesa M, Shirihai OS. Mitochondrial dynamics in the regulation of nutrient utilization and energy expenditure. Cell Metab. 2013;17(4):491-506. Epub 2013/04/09. doi: 10.1016/j.cmet.2013.03.002. PubMed PMID: 23562075; PMCID: PMC5967396.

56. Dar S, Chhina J, Mert I, Chitale D, Buekers T, Kaur H, Giri S, Munkarah A, Rattan R. Bioenergetic Adaptations in Chemoresistant Ovarian Cancer Cells. Sci Rep. 2017;7(1):8760. Epub 2017/08/20. doi: 10.1038/s41598-017-09206-0. PubMed PMID: 28821788; PMCID: PMC5562731.

57. Bellance N, Benard G, Furt F, Begueret H, Smolkova K, Passerieux E, Delage JP, Baste JM, Moreau P, Rossignol R. Bioenergetics of lung tumors: alteration of mitochondrial biogenesis and respiratory capacity. Int J Biochem Cell Biol. 2009;41(12):2566-77. Epub 2009/08/29. doi: 10.1016/j.biocel.2009.08.012. PubMed PMID: 19712747.

58. Ghoneum A, Gonzalez D, Abdulfattah AY, Said N. Metabolic Plasticity in Ovarian Cancer Stem Cells. Cancers (Basel). 2020;12(5). Epub 2020/05/21. doi: 10.3390/cancers12051267. PubMed PMID: 32429566; PMCID: PMC7281273.

59. Yang L, Moss T, Mangala LS, Marini J, Zhao H, Wahlig S, Armaiz-Pena G, Jiang D, Achreja A, Win J, Roopaimoole R, Rodriguez-Aguayo C, Mercado-Uribe I, Lopez-Berestein G, Liu J, Tsukamoto T, Sood AK, Ram PT, Nagrath D. Metabolic shifts toward glutamine regulate tumor growth, invasion and bioenergetics in ovarian cancer. Mol Syst Biol. 2014;10(5):728. Epub 2014/05/07. doi: 10.1002/msb.20134892. PubMed PMID: 24799285; PMCID: PMC4188042.

60. Pasto A, Bellio C, Pilotto G, Ciminale V, Silic-Benussi M, Guzzo G, Rasola A, Frasson C, Nardo G, Zulato E, Nicoletto MO, Manicone M, Indraccolo S, Amadori A. Cancer stem cells from epithelial ovarian cancer patients privilege oxidative phosphorylation, and resist glucose deprivation. Oncotarget. 2014;5(12):4305-19. Epub 2014/06/21. doi: 10.18632/oncotarget.2010. PubMed PMID: 24946808; PMCID: PMC4147325.

61. Denkert C, Budczies J, Kind T, Weichert W, Tablack P, Sehouli J, Niesporek S, Konsgen D, Dietel M, Fiehn O. Mass spectrometry-based metabolic profiling reveals different metabolite patterns in invasive ovarian carcinomas and ovarian borderline tumors. Cancer Res. 2006;66(22):10795-804. Epub 2006/11/17. doi: 10.1158/0008-5472.CAN-06-0755. PubMed PMID: 17108116.

1073 62. Fong MY, McDunn J, Kakar SS. Identification of metabolites in the normal ovary and
1074 their transformation in primary and metastatic ovarian cancer. PLoS One. 2011;6(5):e19963.
1075 Epub 2011/06/01. doi: 10.1371/journal.pone.0019963. PubMed PMID: 21625518; PMCID:
1076 PMC3098284 preliminary analysis of the data and final editing of the manuscript. However, as
1077 part of the University of Louisville's contract with Metabolon, Inc., he does not have any financial
1078 benefit or retention of invention or ownership rights, patentable or not. This does not affect
1079 adherence to PLoS ONE policies on sharing data and material.
1080 63. Mitra K, Wunder C, Roysam B, Lin G, Lippincott-Schwartz J. A hyperfused mitochondrial
1081 state achieved at G1-S regulates cyclin E buildup and entry into S phase. Proc Natl Acad Sci U
1082 S A. 2009;106(29):11960-5. Epub 2009/07/21. doi: 10.1073/pnas.0904875106. PubMed PMID:
1083 19617534; PMCID: PMC2710990.
1084 64. Spurlock B, Parker D, Basu MK, Hjelmeland A, Gc S, Liu S, Siegal GP, Gunter A, Moran
1085 A, Mitra K. Fine-tuned repression of Drp1-driven mitochondrial fission primes a 'stem/progenitor-
1086 like state' to support neoplastic transformation. Elife. 2021;10. Epub 2021/09/22. doi:
1087 10.7554/eLife.68394. PubMed PMID: 34545812; PMCID: PMC8497058.
1088 65. Kong B, Wang Q, Fung E, Xue K, Tsang BK. p53 is required for cisplatin-induced
1089 processing of the mitochondrial fusion protein L-Opa1 that is mediated by the mitochondrial
1090 metallopeptidase Oma1 in gynecologic cancers. J Biol Chem. 2014;289(39):27134-45. Epub
1091 2014/08/13. doi: 10.1074/jbc.M114.594812. PubMed PMID: 25112877; PMCID: PMC4175349.
1092 66. Zou GP, Yu CX, Shi SL, Li QG, Wang XH, Qu XH, Yang ZJ, Yao WR, Yan DD, Jiang
1093 LP, Wan YY, Han XJ. Mitochondrial Dynamics Mediated by DRP1 and MFN2 Contributes to
1094 Cisplatin Chemoresistance in Human Ovarian Cancer SKOV3 cells. J Cancer.
1095 2021;12(24):7358-73. Epub 2022/01/11. doi: 10.7150/jca.61379. PubMed PMID: 35003356;
1096 PMCID: PMC8734405.
1097 67. Tien JF, Mazloomian A, Cheng SG, Hughes CS, Chow CCT, Canapi LT, Oloumi A,
1098 Trigo-Gonzalez G, Bashashati A, Xu J, Chang VC, Shah SP, Aparicio S, Morin GB. CDK12
1099 regulates alternative last exon mRNA splicing and promotes breast cancer cell invasion. Nucleic
1100 Acids Res. 2017;45(11):6698-716. Epub 2017/03/24. doi: 10.1093/nar/gkx187. PubMed PMID:
1101 28334900; PMCID: PMC5499812.
1102 68. Song X, Wan X, Huang T, Zeng C, Sastry N, Wu B, James CD, Horbinski C, Nakano I,
1103 Zhang W, Hu B, Cheng SY. SRSF3-Regulated RNA Alternative Splicing Promotes Glioblastoma
1104 Tumorigenicity by Affecting Multiple Cellular Processes. Cancer Res. 2019;79(20):5288-301.
1105 Epub 2019/08/30. doi: 10.1158/0008-5472.CAN-19-1504. PubMed PMID: 31462429; PMCID:
1106 PMC6801100.

1107 69. Zhu J, Chen Z, Yong L. Systematic profiling of alternative splicing signature reveals
1108 prognostic predictor for ovarian cancer. Gynecol Oncol. 2018;148(2):368-74. Epub 2017/11/27.
1109 doi: 10.1016/j.ygyno.2017.11.028. PubMed PMID: 29191436.
1110 70. He X, Arslan AD, Pool MD, Ho TT, Darcy KM, Coon JS, Beck WT. Knockdown of
1111 splicing factor SRp20 causes apoptosis in ovarian cancer cells and its expression is associated
1112 with malignancy of epithelial ovarian cancer. Oncogene. 2011;30(3):356-65. Epub 2010/09/22.
1113 doi: 10.1038/onc.2010.426. PubMed PMID: 20856201; PMCID: PMC3010329.
1114 71. Shepherd TG, Theriault BL, Campbell EJ, Nachtigal MW. Primary culture of ovarian
1115 surface epithelial cells and ascites-derived ovarian cancer cells from patients. Nat Protoc.
1116 2006;1(6):2643-9. doi: 10.1038/nprot.2006.328. PubMed PMID: 17406520.
1117 72. Li H, Handsaker B, Wysoker A, Fennell T, Ruan J, Homer N, Marth G, Abecasis G,
1118 Durbin R, Genome Project Data Processing S. The Sequence Alignment/Map format and
1119 SAMtools. Bioinformatics. 2009;25(16):2078-9. Epub 2009/06/10. doi:
1120 10.1093/bioinformatics/btp352. PubMed PMID: 19505943; PMCID: PMC2723002.
1121 73. Patro R, Duggal G, Love MI, Irizarry RA, Kingsford C. Salmon provides fast and bias-
1122 aware quantification of transcript expression. Nat Methods. 2017;14(4):417-9. Epub 2017/03/07.
1123 doi: 10.1038/nmeth.4197. PubMed PMID: 28263959; PMCID: PMC5600148.
1124 74. Lam J, Katti P, Biete M, Mungai M, AshShareef S, Neikirk K, Garza Lopez E, Vue Z,
1125 Christensen TA, Beasley HK, Rodman TA, Murray SA, Salisbury JL, Glancy B, Shao J, Pereira
1126 RO, Abel ED, Hinton A, Jr. A Universal Approach to Analyzing Transmission Electron
1127 Microscopy with ImageJ. Cells. 2021;10(9). Epub 2021/09/29. doi: 10.3390/cells10092177.
1128 PubMed PMID: 34571826; PMCID: PMC8465115.
1129 75. Javed Z, Worley BL, Stump C, Shimko SS, Crawford LC, Mythreye K, Hempel N.
1130 Optimization of Extracellular Flux Assay to Measure Respiration of Anchorage-independent
1131 Tumor Cell Spheroids. Bio Protoc. 2022;12(4):e4321. Epub 2022/03/29. doi:
1132 10.21769/BioProtoc.4321. PubMed PMID: 35340292; PMCID: PMC8899553.

1133

1134

Figures

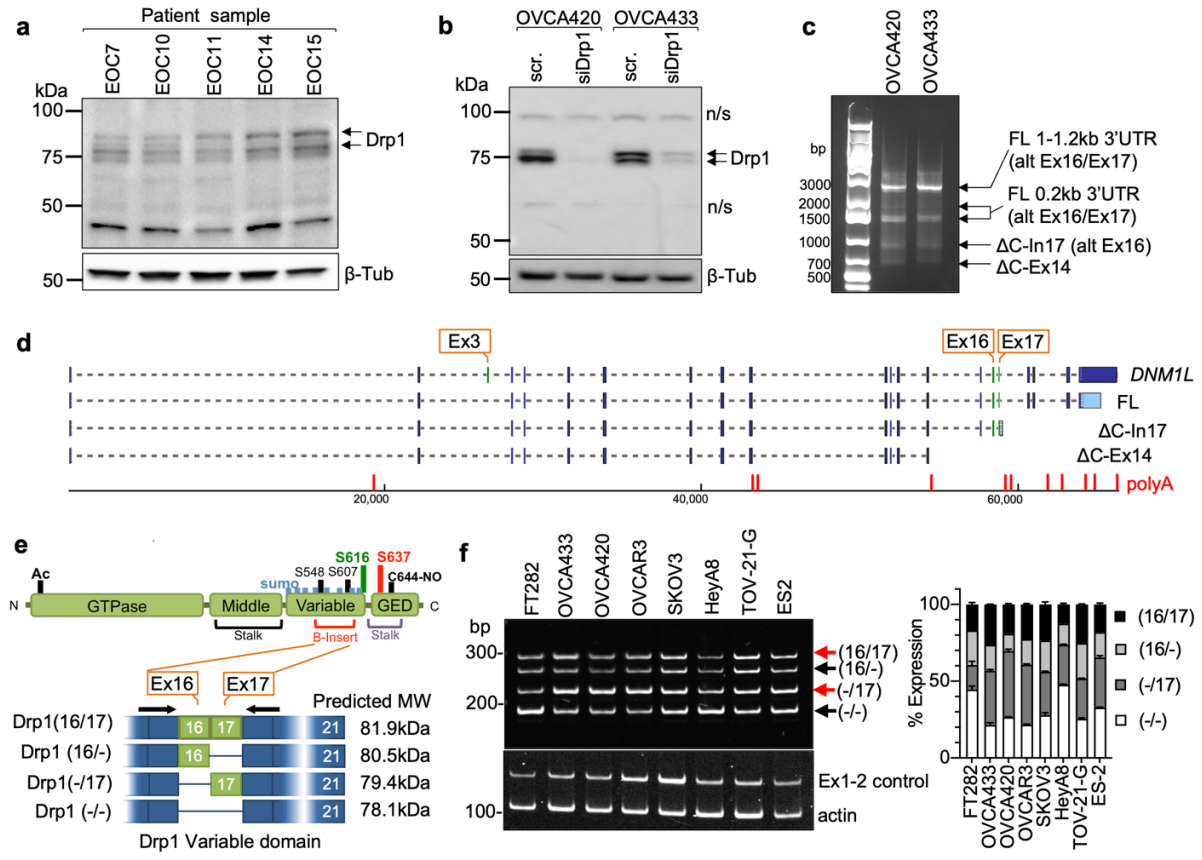

Figure 1. Ovarian cancer cells express splice variants of Drp1/*DNM1L*.

a. Western blot analysis of Drp1 protein expression in patient ascites derived epithelial ovarian cancer cells (EOC), with the following histological classification: EOC7: HGSA stage IC; EOC10: granulosa tumor IV; EOC 11: carcinosarcoma stage IIIB; EOC14: HGSA stage IV; EOC15: HGSA stage IV. Arrows point to the predicted molecular weight protein (upper arrow) and a lower molecular weight band also prominently expressed.

b. Drp1 protein variants identified in OVCA420 and OVCA433 cells by western blotting using N-terminal anti-Drp1 monoclonal antibody ab184247. Specificity to Drp1 was assessed by siRNA mediated knock-down. Potential non-specific bands (n/s) are indicated. One representative blot from 3 independent replicates shown.

c. 3' RACE and subsequent sequencing of PCR products reveals that OVCA420 and OVCA433 cells express multiple *DNM1L* transcripts variants, including full length (FL) transcripts with alternatively spliced exons 16 and 17, and C terminal truncated transcripts at exon 14 (ΔC-Ex14) and intron 17 (ΔC-In17).

d. Schematic of transcript variants identified in OVCA420 and OVCA433 cells by 5' and 3' RACE (c), including alternate splicing of the variable domain exons 16 and 17 (panel c: alt Ex 16/17); variable lengths of 3'UTRs (panel c: FL 1-1.2kb, 0.2kb 3'UTR), and utilization of alternate proximal polyadenylation, resulting in two C terminal truncation variants, terminating in Intron 17 (ΔC-In17) and exon 14 (ΔC-Ex14). ΔC-In17 has two variants due to exon 16 alternate splicing and has a predicted STOP codon following a novel coding sequence for 16 amino acids within intron 17.

e. Schematic representation of the Drp1/*DNM1L* protein sequence functional domains and areas of post-translational modifications. The location of alternate spliced exons 16 and 17 is in the variable B-insert domain. Numbers in brackets of transcript names denote included exons in of the variable domain, dash denotes exon is spliced out.

f. RT-PCR with primers flanking the variable domain illustrates relative expression of the four *DNM1L* variable domain splice variants derived from alternate splicing of exons 16 and 17 in ovarian cancer cell lines (n=3, mean +/- SEM).

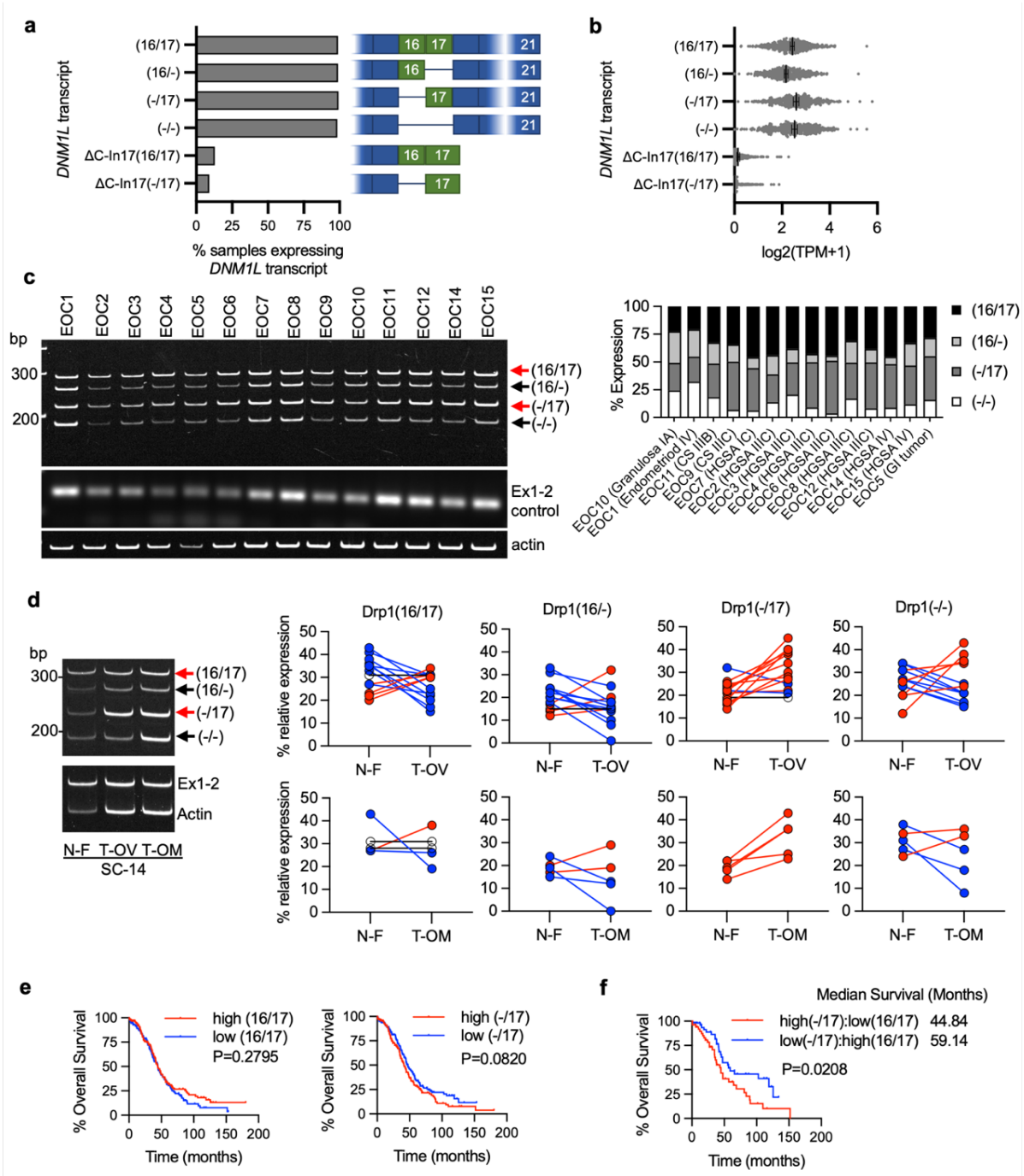

Figure 2. Drp1/*DNM1L* transcript variant expression in ovarian cancer specimens.

a. Frequency of Drp1/*DNM1L* transcript variant expression, focusing on full length variable domain (16/17) transcripts and C terminal truncation terminating in Intron 17 (ΔC-In17). Data represent percentage of specimens displaying TPM values >0.5 for each *DNM1L* transcript variant.

b. Expression levels of *DNM1L* transcript variants from TCGA data.

c. RT-PCR was used to show relative expression of DNM1L variable domain splice variants in a panel of patient ascites derived EOCs. Histologic classification and stage indicated in graph (right; CS: carcinosarcoma; HGSA: high grade serous adenocarcinoma; GI: gastrointestinal).

d. Representative RT-PCR (left) of *DNM1L* variable domain splice variant expression from normal fallopian tube (N-F), and matched ovarian (T-OV) and omental tumors (T-OM). The relative expression of splice variant transcript Drp1(-/17) is consistently higher in ovarian tumor and omental tumor compared to matched

normal fallopian tube specimens (blots see Extended Data Fig. 3; blue lines indicate decreased expression, red lines indicate increased expression and black lines indicate no change in expression relative to matched normal fallopian tube tissue).

e. Overall survival of TCGA patients based on DNM1L variant expression. Samples were split at median log2 TPM into high (n=184) and low expression (n=184; log-rank Mantel-Cox test).

f. Overall survival comparison between samples displaying mutually exclusive high Drp1(-/17)/low Drp1(16/17) (n=52) and low Drp1(-/17)/high Drp1(16/17) (n=52) expression (low and high cutoffs based on median log2 TPM; log-rank Mantel-Cox test).

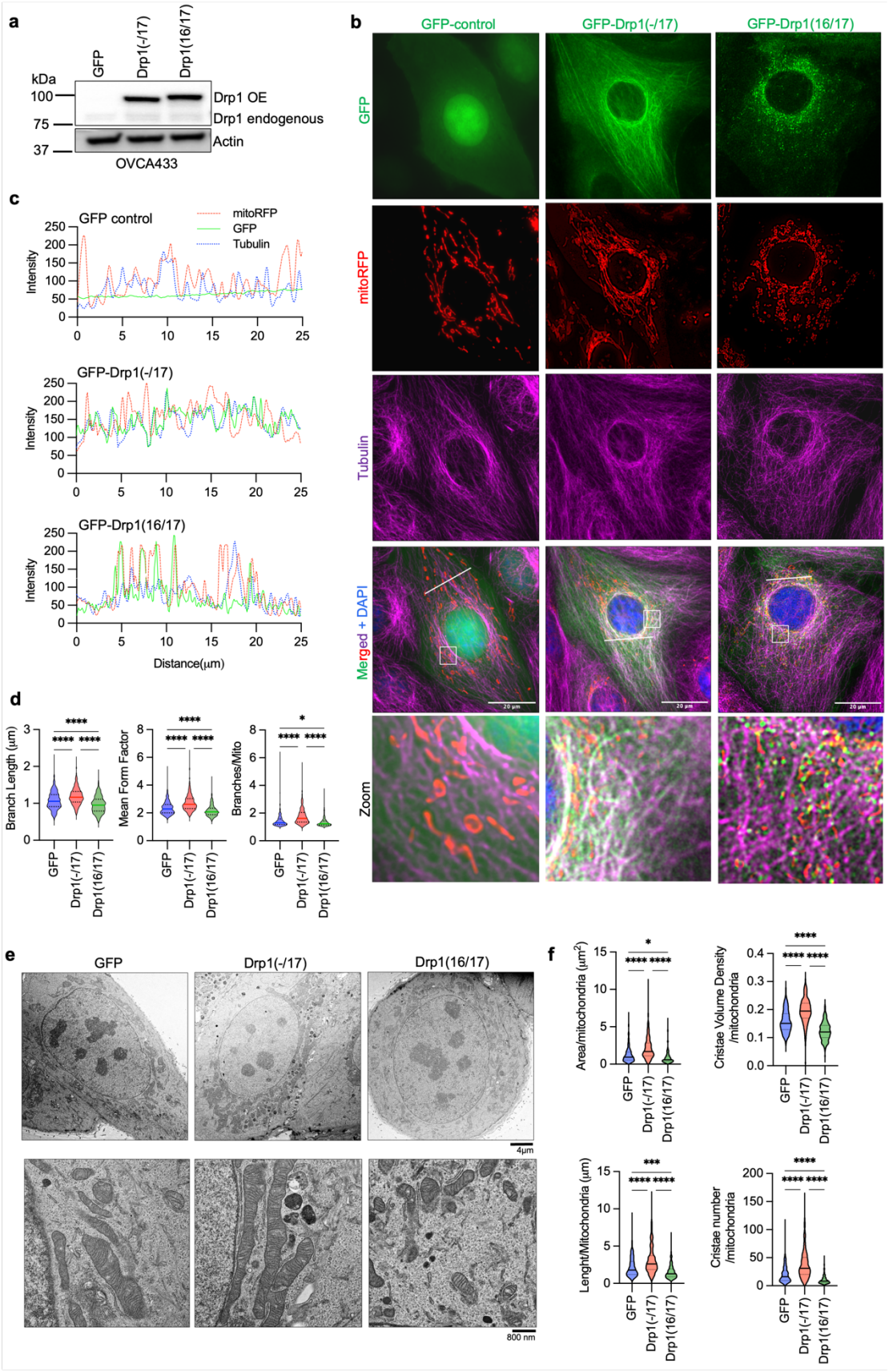

Figure 3. Drp1(-/17) displays decreased association with mitochondria, and its expression increases mitochondrial length and cristae density relative to Drp1(16/17).

a. Western blot analysis following overexpression of GFP-tagged Drp1(-/17), Drp1(16/17) GFP vector control in OVCA433 cells.

b. Representative epifluorescence images of mitochondrial morphology and Drp1 distribution in OVCA433 cells. (Green: GFP or GFP-tagged Drp, Red: mito-RFP to label mitochondria, Magenta: Tubulin immunostained with anti-Tubulin antibody and Blue: DAPI). Drp1(-/17) shows a distinct pattern of co-localization with Tubulin, differing from the traditional punctate staining of Drp1 at mitochondria, a characteristic observed with Drp1(16/17). Scale bar: 20 μm.

c. Representative histograms of fluorescence intensity (white line in images on right) illustrate that Drp1(-/17) (green) is more closely aligned with Tubulin (blue) and less so with mitochondria (red), pointing towards reduced mitochondria association. In contrast, Drp1(16/17) peaks coincide with mitochondrial (red) peaks, reflective of Drp1 mitochondrial fission puncta.

d. Drp1(-/17) expressing cells show a decrease in fission, evidenced by the presence of a more elongated and branched network of mitochondria than in cells expressing Drp1(16/17). Quantification of mitochondrial morphological represented by three independent descriptors as analyzed by mitochondria analyzer in ImageJ. n = 498 cells from GFP-control, n = 568 cells from Drp1(-/17) and n=553 cells from Drp1(16/17) were analyzed. (one-way ANOVA Mean Form Factor $p < 0.0001$; Branch Length $p < 0.0001$ and Branches/mito $p<0.0001$. Tukey's post test *$p<0.05$, ****$p < 0.0001$).

e. Drp1(-/17) expressing cells have more fused mitochondria with greater cristae organization and volume. Representative Transmission EM images of OVCA433 cells. Arrows indicate the elongated mitochondria in Drp1(-1/7), fragmented mitochondria in Drp1(16/17) and a range of elongated to fragmented mitochondria in GFP cells. Scale bar: 4 μm and 800nm

f. Quantification of mitochondria and cristae from TEM images. magnification 800nM. n =156 cells from GFP-control, n =160 cells from Drp1(-/17) and n=157 cells from Drp1(16/17) were analyzed. (one-way ANOVA Area/mitochondria $p<0.0001$, Cristae volume density $p<0.0001$, Length/mitochondria $p<0.0001$ and Cristae number/mitochondria $p<0.0001$. Tukey's post test *$p < 0.05$, ***$p < 0.001$, ****$p < 0.0001$).

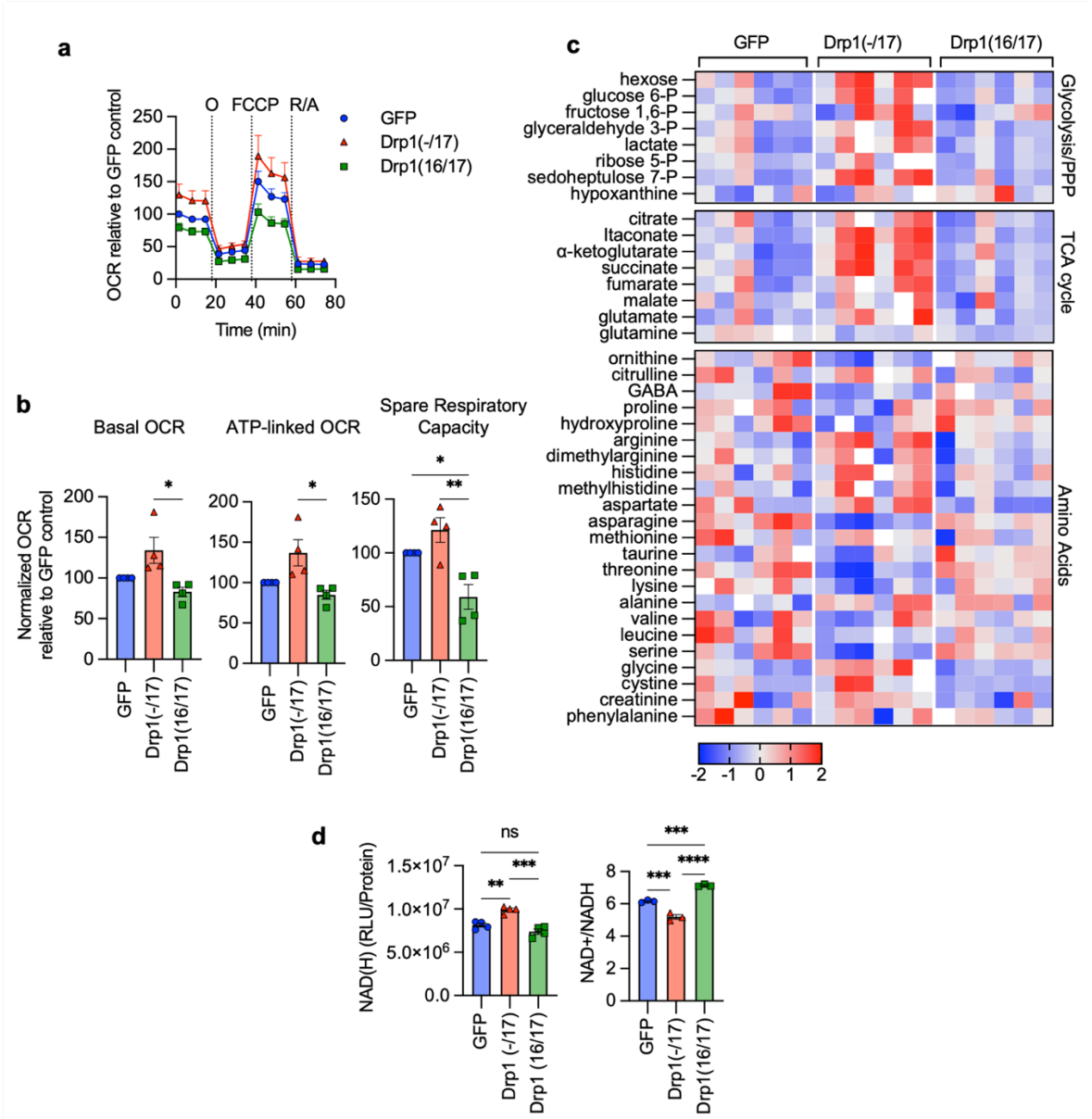

Figure 4. Expression of Drp1(-/17) splice variant increases mitochondrial respiration and TCA cycle metabolites.

a. Expression of Drp1(-/17) increases oxygen consumption rates (OCR) in OVCA433 cells as assessed by mitochondrial stress test using Seahorse extracellular flux analysis (O: oligomycin A, R/A: rotenone/antimycin A; OCR is normalized to cell viability and expressed relative to GFP control, n=4)

b. Basal OCR, ATP-linked OCR and spare respiratory capacity are increased in OVCA433 cells expressing Drp1(-/17) compared to Drp1(16/17). Data are expressed relative to GFP control (n=4, one-way ANOVA Basal OCR p=0.0144; ATP-linked OCR p=0.0131; spare respiratory capacity p=0.0034; Tukey's post test **p<0.01, ***p<0.001, ****p<0.0001)

c. Relative metabolite content of OVCA433 cells stably expressing GFP control, GFP-Drp1(-/17) or GFP-Drp1(16/17) as assessed by untargeted LC-HRMS (n=6, heatmap reflects z-scores of Area/iSTD values).

d. Total NAD(H) levels are increased in response to Drp1(-/17) expression relative to OVCA433 cells expressing GFP control or Drp1(16/17), while the ratio of NAD+/NADH is significantly decreased (one-way ANOVA NAD(H) n=4, p=0.0002; NAD+/NADH n=3 p<0.0001; Tukey's post test **p<0.01, ***p<0.001, ****p<0.0001).

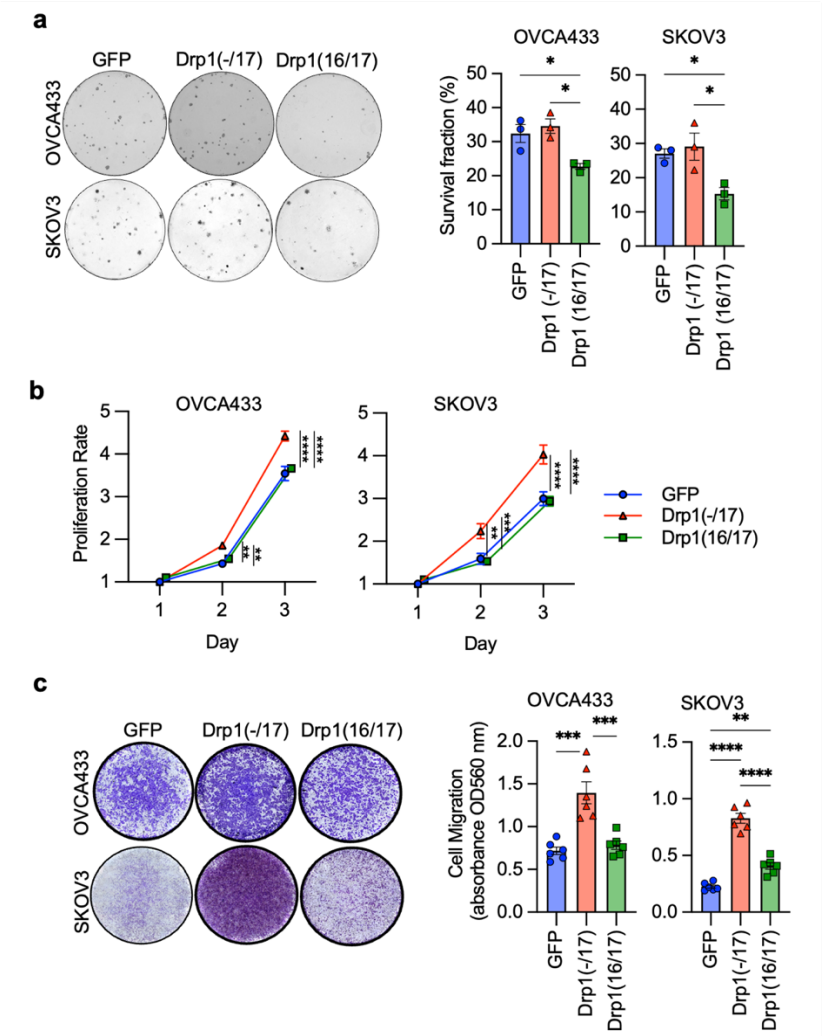

Figure 5. Compared to Drp1(16/17), expression of Drp1(-/17) maintains clonogenic survival, promotes proliferation and migration of ovarian cancer cells.

a. Drp1(16/17) expression lowers single cell clonogenic survival in both OVCA433 and SKOV3 cells. Cells (100/well) were seeded onto 6-well plates and stained with crystal violet after 7-10 days in culture. Colonies were quantified using ImageJ. Images are representative of 3 independent experiments (n=3, one-way ANOVA OVCA433 p=0.0128; SKOV3 p=0.0201. Tukey's post test *p<0.05).

b. Compared to Drp1(16/17) and GFP expression, Drp1(-/17) increases proliferation rate of OVCA433 and SKOV3 cells. Cell proliferation was assessed by FluoReporter dsDNA quantification and proliferation rate expressed as increase in the cell density relative to day 1 (n=3, two-way ANOVA group factor variance p<0.0001, Tukey's post test **p < 0.01, ***p < 0.001 and ****p < 0.0001).

c. Drp1 variants differently alter cell migration, with Drp1(-/17) expressing cells showing greater migratory ability than Drp1(16/17) or GFP control expressing cells. Cell migration was assessed using the Boyden chamber transwell assay and quantified by measuring the absorbance of the crystal violet staining of migrated cells. Images are representative of 3 independent assays (n=3, one-way ANOVA OVCA433 p=0.0155; SKOV3 p=0.0003. Tukey's post test *p<0.05, **p < 0.01. and ***p < 0.001).

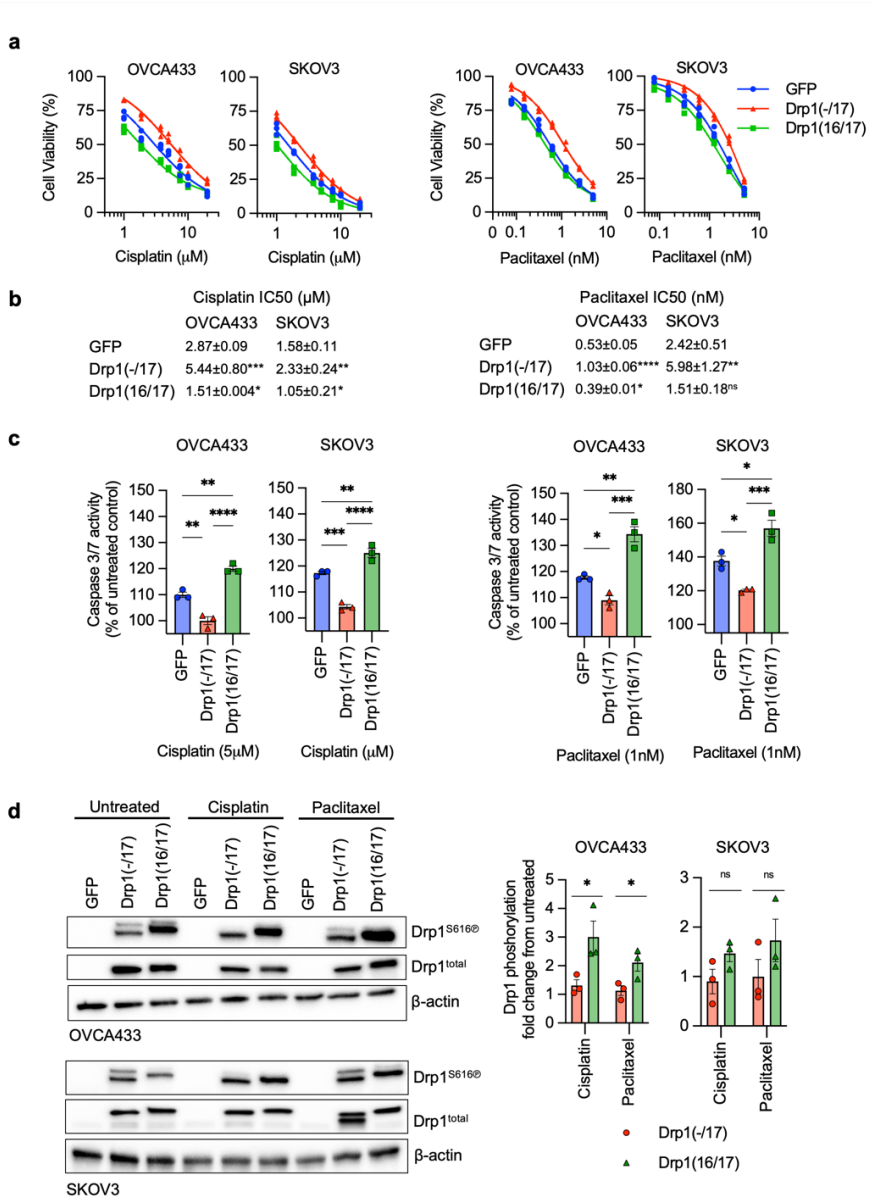

Figure 6. Expression of Drp1(-/17) decreases sensitivity to chemotherapeutics.

a. Dose response curves were derived from cell viability assays in response to cisplatin and paclitaxel treatment of OVCA433 and SKOV3 cells expressing GFP vector control, Drp1(-/17) and Drp1(16/17). Cells were plated into 96 wells and were exposed to increasing concentrations of cisplatin and paclitaxel for 72 hours respectively. Cell viability expressed as survival fraction was assessed by FluoReporter dsDNA quantification (n=3).

b. IC50 values were calculated from the above curves (n=3, one way ANOVA, Dunnet's post test comparison to GFP control *p<0.05, **p<0.01, ***p<0.001, ***p<0.0001).

c. Cells expressing Drp1(-/17) display abrogated apoptosis in response to cisplatin (5 μM) or paclitaxel (1 nM) treatment after 24 hours, as assessed using Caspase-Glo 3/7 assay (n=3, one-way ANOVA cisplatin OVCA433 p=<0.0001, SKOV3 p=<0.0001; paclitaxel OVCA433 p=0.0003, SKOV3 p=0.0006. Tukey's post test *p<0.05, **p<0.01, ***p<0.001, ****p<0.0001).

d. S616 phosphorylation of recombinant expressed Drp1 following cisplatin (5 μM) and paclitaxel (1 nM) treatment, as assessed by western blotting.

e. Change in Drp1 phosphorylation (S616) in response to cisplatin (5 μM) and paclitaxel (1 nM) is expressed relative to untreated control (Densitometry quantification was carried out using ImageJ and normalizing to total Drp1, n=3, unpaired t test *p<0.05).

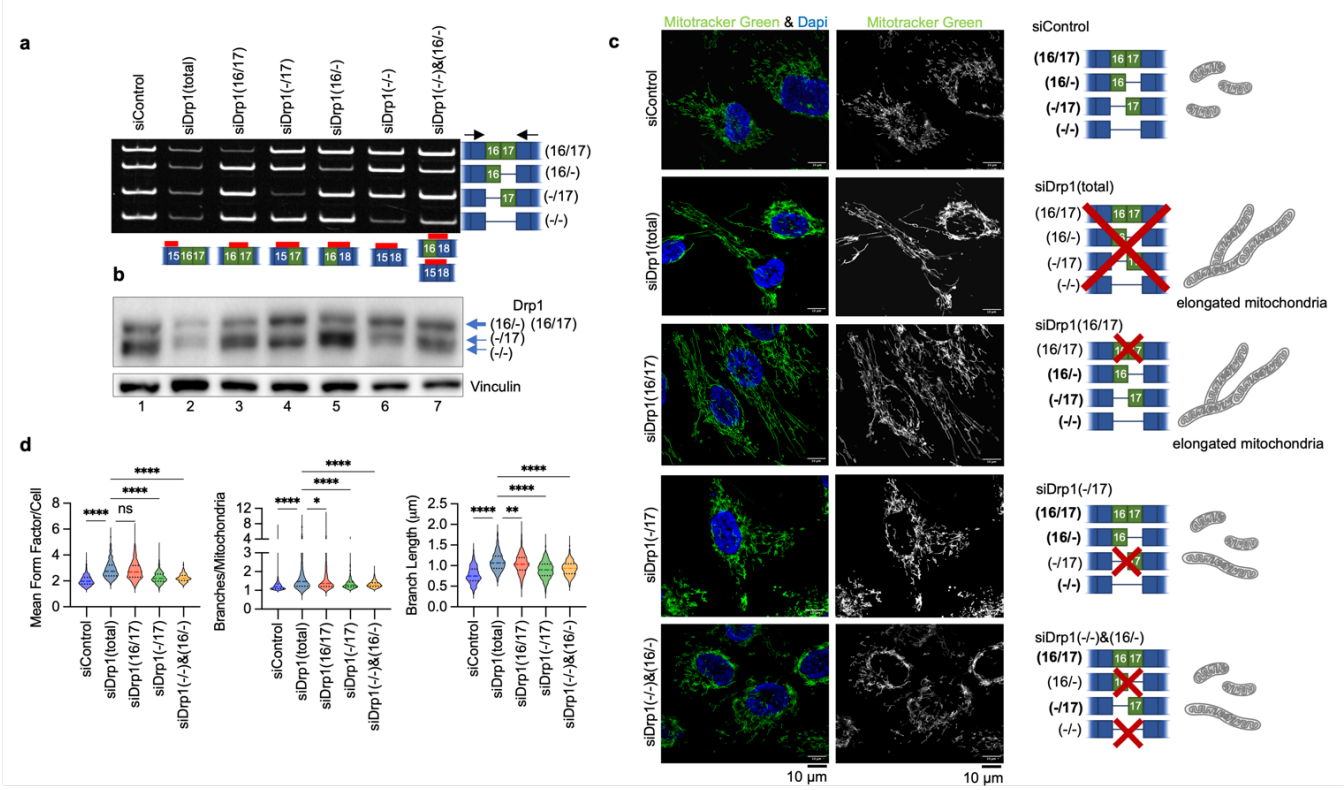

Figure 7. Specific knock-down of endogenous Drp1 splice variants using siRNA and effects on mitochondrial morphology.

a. RT-PCR demonstrating variant specific knock-down of Drp1 using splice variant specific siRNA in SKOV3 cells. One representative gel from independent replicates shown.

b. Splice variant specific siRNA mediated knock down of Drp1 protein in SKOV3 cells by western blotting. One representative blot from 3 independent replicates shown.

c. Representative epifluorescence images of mitochondrial morphology upon splice variant specific siRNA Drp1 knockdown in SKOV3 cells. (Green: mitotracker green and Blue: DAPI). The disruption of endogenous Drp1 splice variant expression differentially modifies mitochondrial dynamics. siDrp1(16/17) most closely replicates the elongated mitochondrial morphology observed following knock-down of all Drp1 variants (siDrp1 total), whereas siDrp1(-/17), and siDrp1(-/-)&(16/-) combination knock-down affect mitochondrial length and networking to a lesser degree. Scale bar: 10 µm.

d. Quantification of mitochondrial morphological represented by three independent descriptors as analyzed by mitochondria analyzer (ImageJ, analysis performed on sicontrol n = 560 cells, siDrp1(total) n = 334, siDrp1(16/17) n=630, siDrp1(-/17) n=655, siDrp1(-/-)&(16/-) n=555; one-way ANOVA Mean Form Factor $p < 0.0001$; Branch Length $p < 0.0001$ and Branches/mito $p<0.0001$. Tukey's post test was performed to assess differences between groups and comparisons of groups relative to siDrp1(total) are shown, *$p<0.05$, **$p<0.01$, ****$p < 0.0001$).

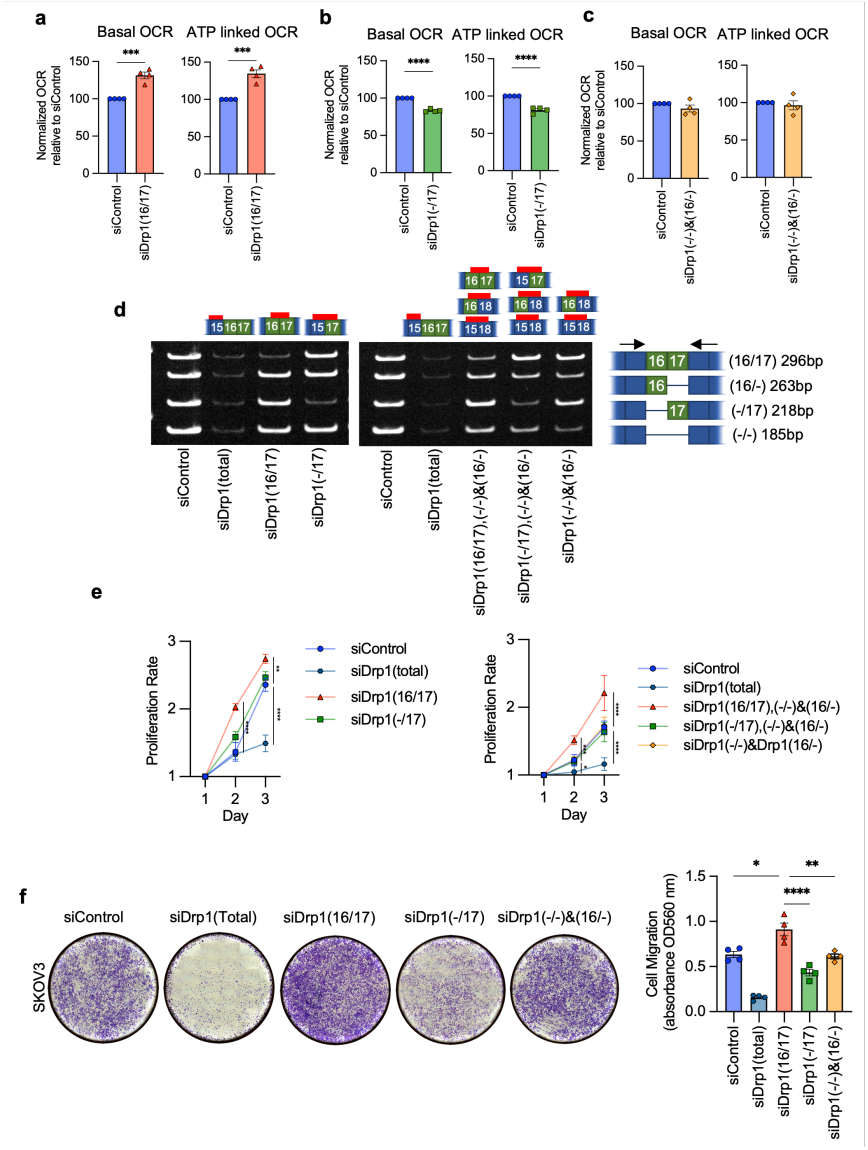

Figure 8. Targeted knock-down of endogenous Drp1 splice variants in SKOV3 cells differentially affect mitochondrial respiration, proliferation and migration.

a. Basal and ATP OCR indicating Mitochondrial respiration improved upon siRNA mediated knock down of the Drp1(16/17) splice variant, as assessed by mitochondrial stress test using Seahorse extracellular flux analysis (n=4, unpaired t-test. ***p<0.001).

b. Conversely, specific knock down of Drp1(-/17) decreased basal and ATP OCR indicating lower mitochondrial respiration (n=4, unpaired t-test. ****p<0.0001; OCR: oxygen consumption rate).

c. Mitochondrial respiration unchanged by combination Drp1(16/-) and (Drp1(-/) knock-down relative to siControl cells (n=4).

d. RT-PCR demonstrating knock-down of Drp1 using single splice variant specific siRNA or combination of splice variant specific siRNA enriching single Drp1 variant in cells to study cell proliferations changes with altered endogenous Drp1 variants. One representative gel from independent replicates shown.

e. Single variant knock-down of Drp1(16/17) and Drp1(-/17) variant enrichment with combination knock-down increases proliferation rate of SKOV3 cells relative to siControl. Cell proliferation was assessed by FluoReporter dsDNA quantification and proliferation rate expressed as increase in the cell density relative to day 1. (n=3, two-way ANOVA group factor variance p<0.0001, Tukey's post test was performed to assess

differences between groups and analysis comparing groups are shown, *p < 0.05, **p < 0.01, ***p < 0.001 and ****p < 0.0001).

f. Endogenous Drp1 splice variants differentially effect cell migration in SKOV3 cells, with siDrp1(16/17) increasing migratory ability while in contrast siDrp1(-/17) reduced cell migration than siControl cells. Post variant specific Drp1 knock-down, cell migration was assessed using the Boyden chamber transwell assay and quantified by measuring the absorbance of the crystal violet staining of migrated cells. Images are representative of 4 independent assays (n=4, one-way ANOVA ****p<0.0001. Tukey's post test was performed to assess differences between groups and analysis comparing siControl, siDrp1(16/17), siDrp1(-/17) and siDrp1(-/-)&(16/-) groups are shown, Tukey's multiple comparison *p<0.05, **p < 0.01. and ****p < 0.0001).

Extended Data Figures

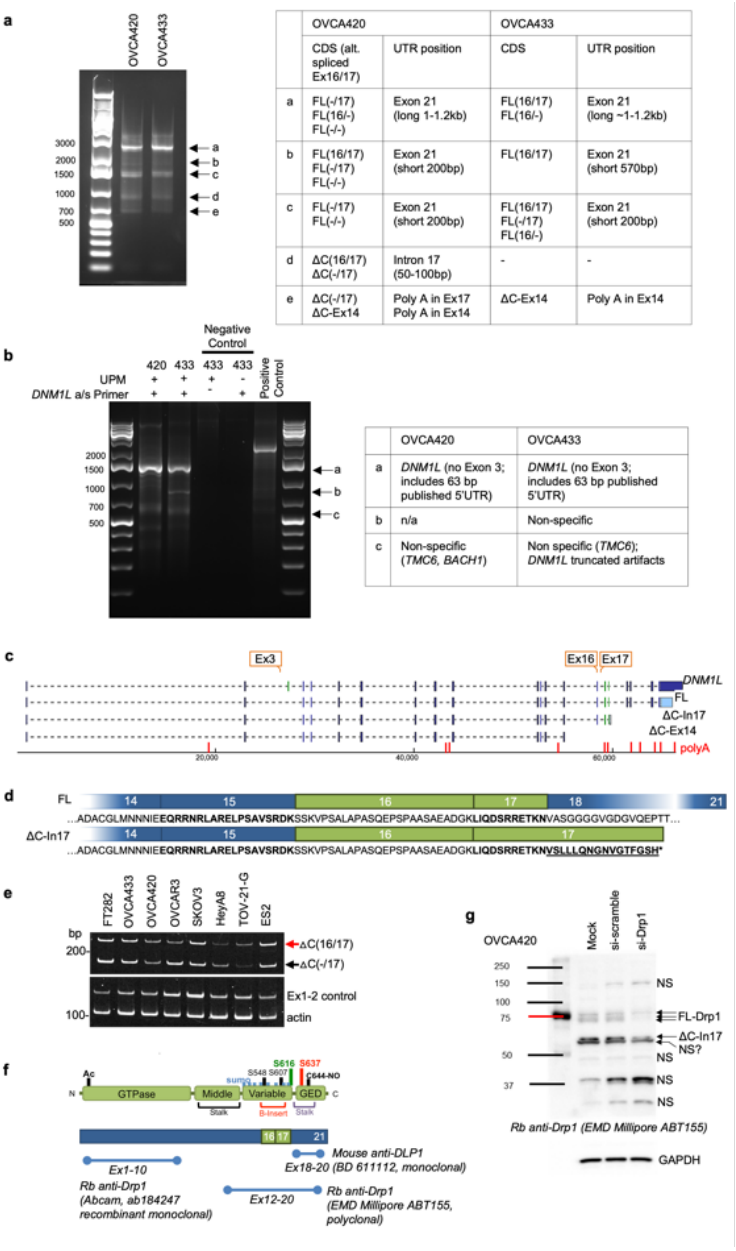

	OVCA420		OVCA433	
	CDS (alt. spliced Ex16/17)	UTR position	CDS	UTR position
a	FL(-/17) FL(16/-) FL(-/-)	Exon 21 (long 1-1.2kb)	FL(16/17) FL(16/-)	Exon 21 (long ~1-1.2kb)
b	FL(16/17) FL(-/17) FL(-/-)	Exon 21 (short 200bp)	FL(16/17)	Exon 21 (short 570bp)
c	FL(-/17) FL(-/-)	Exon 21 (short 200bp)	FL(16/17) FL(-/17) FL(16/-)	Exon 21 (short 200bp)
d	ΔC(16/17) ΔC(-/17)	Intron 17 (50-100bp)	-	-
e	ΔC(-/17) ΔC-Ex14	Poly A in Ex17 Poly A in Ex14	ΔC-Ex14	Poly A in Ex14

	OVCA420	OVCA433
a	*DNM1L* (no Exon 3; includes 63 bp published 5'UTR)	*DNM1L* (no Exon 3; includes 63 bp published 5'UTR)
b	n/a	Non-specific
c	Non-specific (*TMC6, BACH1*)	Non specific (*TMC6*); *DNM1L* truncated artifacts

Extended Data Figure 1. Identification of Drp1 transcript variants in ovarian cancer cell lines.

a. 3' RACE reveals that ovarian cancer cell lines OVCA420 and OVCA433 express multiple Drp1/*DNM1L* transcripts variants, including full length (FL) transcripts with alternatively spliced exons 16 and 17, and C terminal truncated transcripts at exon 14 (ΔC-Ex14) and intron 17 (ΔC-In17). 3' RACE was carried out using SMARTer 3'5'RACE kit (Takara). PCR products from each cell line (a-e) were gel-extracted and cloned into the in-Fusion pRACE vector. 3-5 colonies per clone were selected for sequencing to determine the major5'RACE products in OVCA420 and OVCA433 cells (Table).

b. 5' RACE reveals that *DNM1L* transcripts expressed in OVCA420 and OVCA433 cell share the same 5'UTR and lack exon 3. 5' RACE was carried out using SMARTer 3'RACE kit (Takara) the with the Universal Primer A Mix (UPM) and the *DNM1L* specific antisense primer, positioned in Exon 12. PCR products from each cell line (a-c) were gel-extracted and cloned into the in-Fusion pRACE vector. 3-5 colonies per clone

were selected for sequencing to determine the major 5'RACE products in OVCA420 and OVCA433 cells (Table).

c. Transcript variants identified in OVCA420 and OVCA433 cells include alternate splicing of the variable domain exons 16 and 17; variable lengths of 3'UTRs, and utilization of proximal polyadenylation, resulting in two C terminal truncation variants, terminating in Intron 17 (ΔC-In17) and exon 14 (ΔC-Ex14; indicated in red; PolyA_DB v.3.2; PolyASites). 5'RACE demonstrated that ovarian cancer cell lines cell share the same 5'UTR and lack exon 3.

d. Schematic of the *DNM1L* variable domain Exons 16 and 17 alternatively spliced in ovarian cancer cells and corresponding amino acid sequences. The variant terminating in Intron 17 (ΔC-In17) also displays variable domain exon 16 alternate splicing and is predicted to encode an additional 16 amino acids from the adjacent intron to terminate at an alternate STOP codon.

e. RT-PCR with primers designed to detect the intronic retention of the 3' region of ΔC-In17 illustrates that the *DNM1L* C terminal truncation variant terminating in Intron 17 can be detected in most ovarian cancer cell lines to variable degrees and that these transcripts can vary in their splicing of exon 16.

f. Position of epitopes used to generate commercially available Drp1 antibodies. Note that C-terminal targeted antibody BD611112 is predicted not to recognize potential C-terminal truncations.

g. Protein variants identified in the range of 65-80kDa by western are verified to be Drp1 by siRNA mediated knock-down. Non-specific bands (n/s) are not affected by siRNA against Drp1.

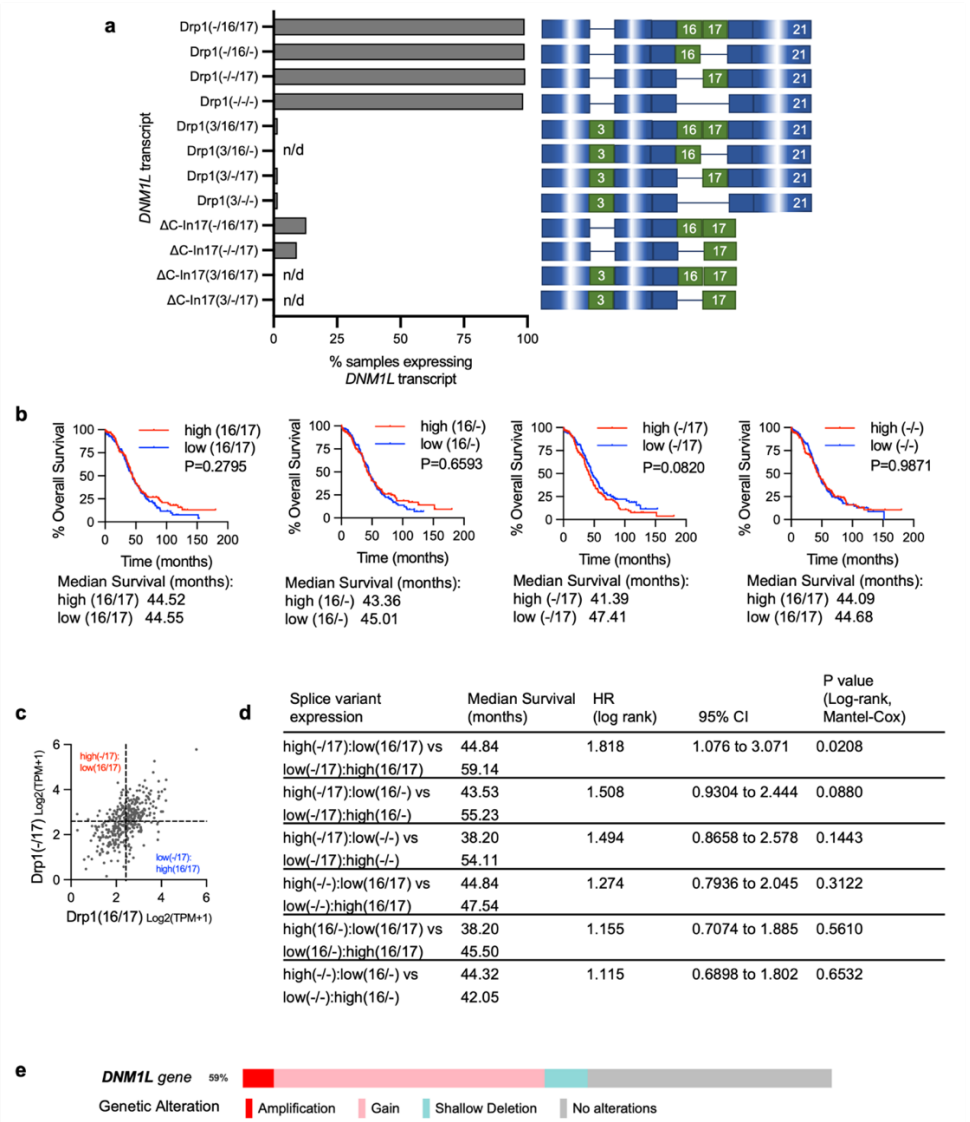

Splice variant expression	Median Survival (months)	HR (log rank)	95% CI	P value (Log-rank, Mantel-Cox)
high(-/17):low(16/17) vs low(-/17):high(16/17)	44.84 59.14	1.818	1.076 to 3.071	0.0208
high(-/17):low(16/-) vs low(-/17):high(16/-)	43.53 55.23	1.508	0.9304 to 2.444	0.0880
high(-/17):low(-/-) vs low(-/17):high(-/-)	38.20 54.11	1.494	0.8658 to 2.578	0.1443
high(-/-):low(16/17) vs low(-/-):high(16/17)	44.84 47.54	1.274	0.7936 to 2.045	0.3122
high(16/-):low(16/17) vs low(16/-):high(16/17)	38.20 45.50	1.155	0.7074 to 1.885	0.5610
high(-/-):low(16/-) vs low(-/-):high(16/-)	44.32 42.05	1.115	0.6898 to 1.802	0.6532

Extended Data Figure 2. Drp1/*DNM1L* transcript variant expression in ovarian cancer specimens from TCGA.

a. Frequency of Drp1/*DNM1L* transcript variant expression, focusing on full length transcpri variants and alternatively spliced exons 3, 16 and 17 (3/16/17) transcripts and C terminal truncation terminating in Intron 17 (ΔC-In17). Dash denotes exon is spliced out. Data represent percentage of specimens displaying log2 TPM+1 values >0.5 for each DNM1L variant.

b. Overall survival of TCGA patients based on DNM1L variant expression. Samples were split at median log2 TPM into high (n=184) and low expression (n=184; log-rank Mantel-Cox test).

c. Drp1(-/17) expression relative to Drp1(16/17; log2 TPM+1). Mutually exclusive high and low expression of variant pairs is based on median log2 TPM+1 expression cut offs indicated by dotted line.

d. Overall survival data of TCGA ovarian cancer patients grouped into mutually exclusive high/low expression of Drp1 transcript variant pairs. Low and high cutoffs based on median expression. Patients with high Drp1(-/17) and low Drp1(16/17) expression display significantly decreased overall survival compared to patients with high Drp1(16/17) and low Drp1(-/17) transcript levels in their tumors.

e. *DNM1L* gene copy number alterations in 233 Ovarian Serous Cystadenocarcinoma cases with complete CNA data (TCGA, PanCancer Atlas). 5% of cases display high level amplification, 46% low level gain, and 7% shallow deletion.

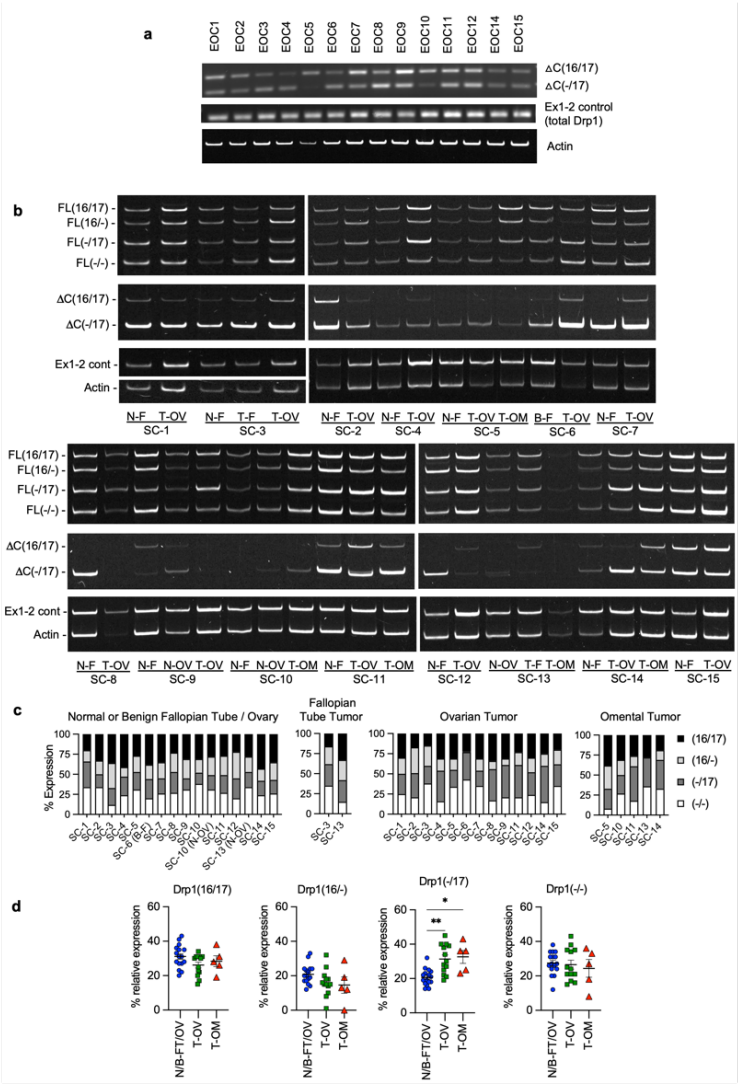

Extended Data Figure 3. ***Expression of DNM1L splice variants in matched patient specimens*.**

a. RT-PCR was used to show relative expression of ΔC(-/17) and ΔC(16/17) truncated transcripts of DNM1L in a panel of patient ascites derived EOCs. (EOC9 & 11: carcinosarcoma; EOC 2,3,4 HGSA high grade serous adenocarcinoma; GI: gastrointestinal; tumor stage is indicated in Figure 2c).

b. RT-PCR of *DNM1L* variable domain splice variant expression from normal fallopian tube (N-F), and matched ovarian (T-OV) and omental tumors (T-OM). The relative expression of splice variant transcript Drp1(-/17) is consistently higher in ovarian tumor and omental tumor compared to matched normal fallopian tube specimens N=normal, T=tumor, B=benign, F=fallopian tube, OV= ovary, OM= omentum. All specimens were classified as HGSA, and the following stage: SC-1: IIIC, SC-2: IIIB, SC-3: IIIC, SC-4: IB, SC-5: IIIC, SC-6: IC3, SC-7: IIIB, SC-8: IIIC, SC-9: IVB, SC-10: IIIC, SC-11: IIIB, SC-12: IC2, SC-13: IIIC, SC-14: IIIC, SC-15: IIIB.

c. Quantification of relative Drp1 variable domain splice variant expression from panel b.

d. Comparison of relative expression of each variant between normal fallopian tube/ovary and ovarian tumor or omental tumor. Relative expression of Drp1(-/17) compared to other variants is significantly increased in ovarian tumors and omental tumors compared to matched normal tissues. (Mixed Effects Analysis with Tukey's post test. *p<0.05, **p<0.01).

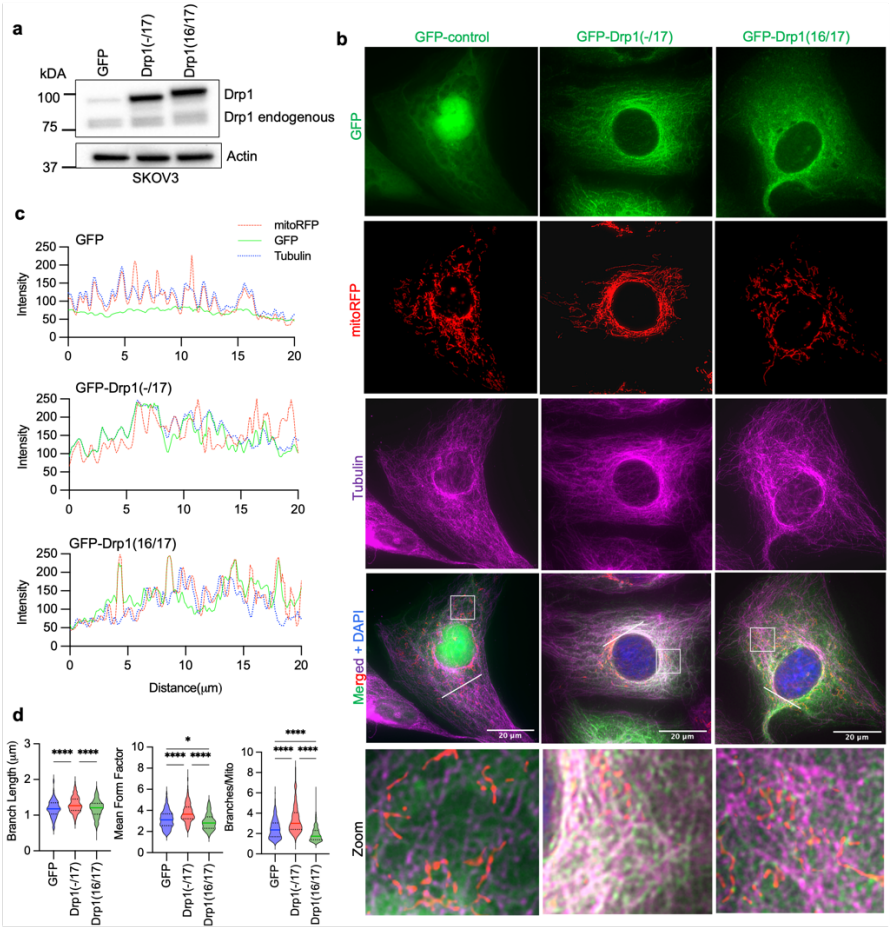

Extended Data Figure 4: Drp1(-/17) displays decreased association with mitochondria and increased localization to microtubules in SKOV3 cells.

a. Western blot analysis of GFP-tagged Drp1 protein expression in SKOV3 cells.

b. Representative epifluorescence images of mitochondrial morphology and Drp1 distribution in SKOV3 cells. (Green: GFP or GFP-tagged Drp, Red: mitochondria traced with mito-RFP, Magenta: Tubulin immunostained with anti-Tubulin antibody and Blue: DAPI). Drp1(-/17) expression in SKOV3 cells also shows a greater degree of co-localization with Tubulin as opposed to mitochondria, a contrast to the expression of Drp1(16/17), which exhibits the more traditional fission punctate staining at the mitochondria. Scale bar: 20 µm.

c. Representative histograms of fluorescence intensity (white line in images on right) illustrate that Drp1(-/17) (green) is more closely aligned with Tubulin (blue) and less so with mitochondria (red), pointing towards reduced mitochondria association. In contrast, Drp1(16/17) peaks coincide with mitochondrial (red) peaks, indicative of the Drp1 mitochondrial fission puncta.

d. Drp1(-/17) expression in SKOV3 exhibit diminished fission, as illustrated by their more elongated and interconnected mitochondrial network, in contrast to cells that express Drp1(16/17). Quantification of mitochondrial morphological represented by three independent descriptors as analyzed by mitochondria analyzer in ImageJ. n = 180 cells from GFP-control, n = 224 cells from Drp1(-/17) and n=252 cells from Drp1(16/17) were analyzed. (one-way ANOVA Mean Form Factor p <0.0001; Branch Length p <0.0001and Branches/mito p <0.0001. Tukey's post test *p<0.05, ****p <0.0001).

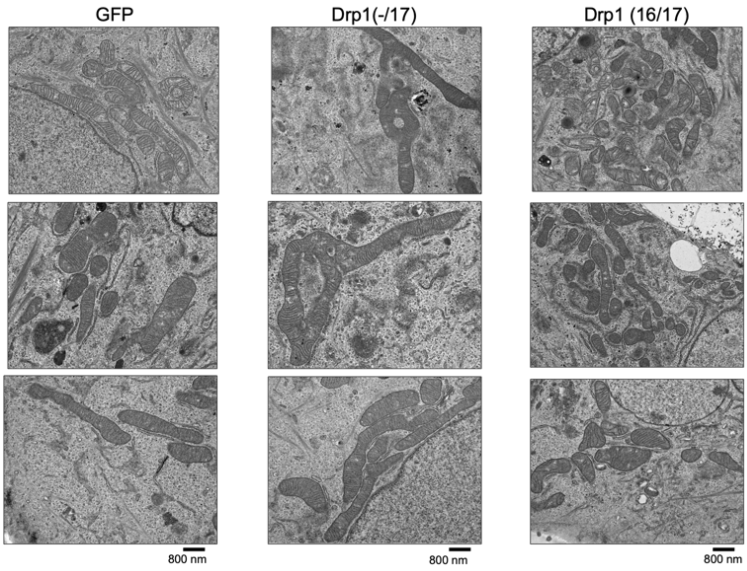

Extended Data Figure 5: Drp1(-17) and Drp1(16/17) expression differentially alter mitochondrial architecture of OVCA433 cells.

Representative TEM images from 3 individual biological replicates demonstrate a more fused mitochondrial morphology in Drp1(-/17) cells compared to the smaller, fragmented mitochondria characteristic of Drp1(16/17) cells. Meanwhile, mitochondria in GFP control cells exhibit a variety of forms, from elongated to smaller, fragmented shapes. Scale bar: 800nm.

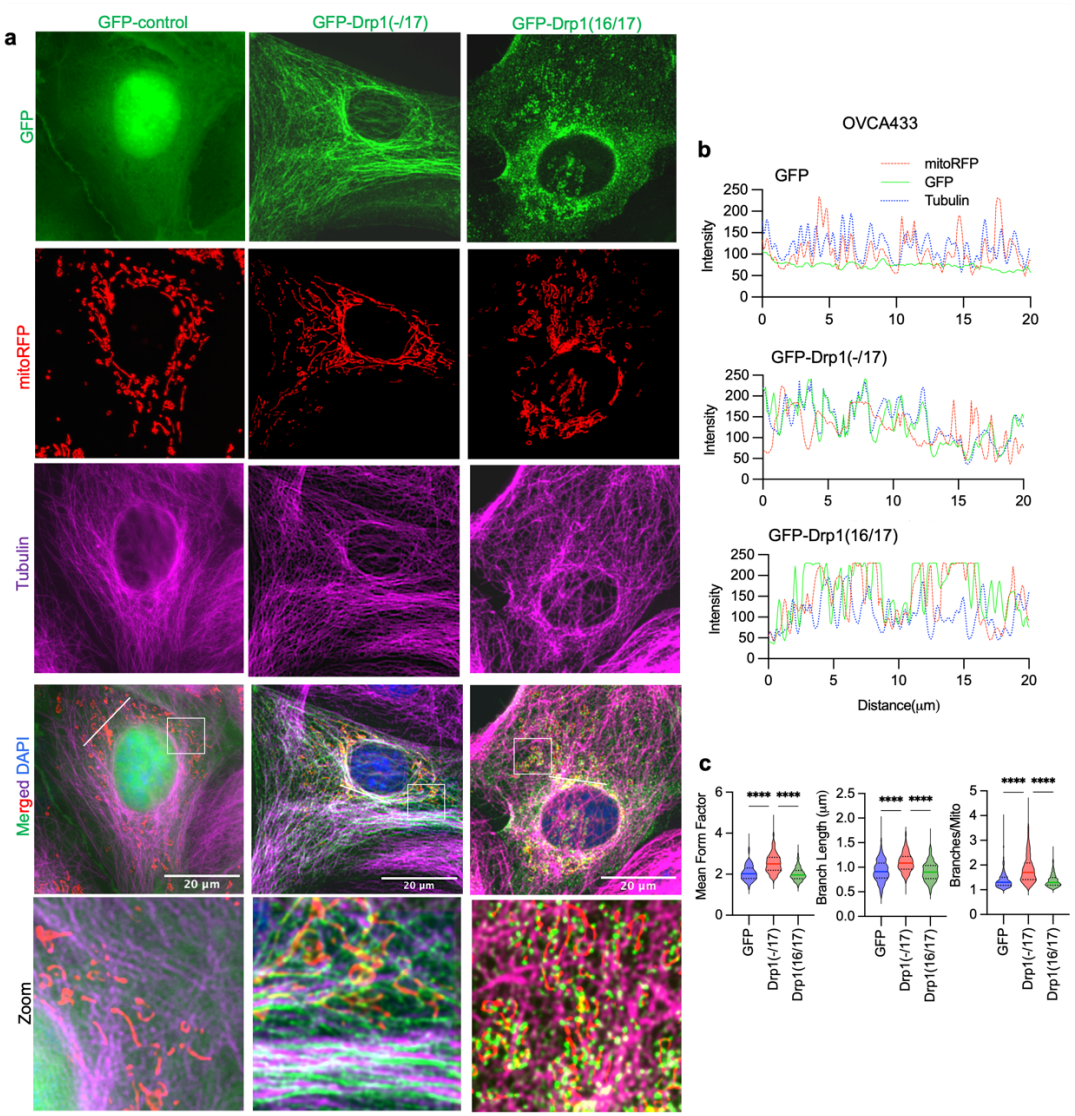

Extended Data Figure 6. Drp1(-/17) displays decreased association with mitochondria in response to FCCP.

a. Drp1(-/17) preserves its localization with Tubulin even upon treatment with the fission stimulus FCCP. In contrast, Drp1(16/17) cells have increased fission puncta staining at mitochondria in response to FCCP. Representative epifluorescence images of mitochondrial morphology and Drp1 distribution after 30 minutes with FCCP treatment (1µM) in OVCA433 cells. (Green: GFP or GFP-tagged Drp1, Red: mitochondria targeted RFP, Magenta: anti-Tubulin, Blue: DAPI; Scale bar: 20 µm).

b. Representative histogram of fluorescence intensity (white line in images on right) of GFP-Drp1 (green) in conjunction with mitochondria (red) and Tubulin (blue), illustrates that GFP-Drp1(16/17) strongly overlaps with mitochondria following FCCP treatment (1 µM, 30 mins). Conversely, Drp1(-/17) even with a pro-fission stimulus has higher overlapping peaks with tubulin than mitochondria, demonstrating decreased mitochondrial association.

c. Drp1(16/17) and GFP control cells show the anticipated reduction in mitochondrial size and increased fragmentation with FCCP, in contrast to Drp1(-/17) cells which continue to maintain elongated mitochondria. Quantification of mitochondrial morphological represented by three independent descriptors as analyzed by mitochondria analyzer in ImageJ. n = 301 cells from GFP-control, n = 285 cells from Drp1(-/17) and n=287 from Drp1(16/17) were analyzed. (one-way ANOVA Mean Form Factor p <0.0001; Branch Length p <0.0001 and Branches/mito p<0.0001. Tukey's post test *p<0.05, ****p <0.0001).

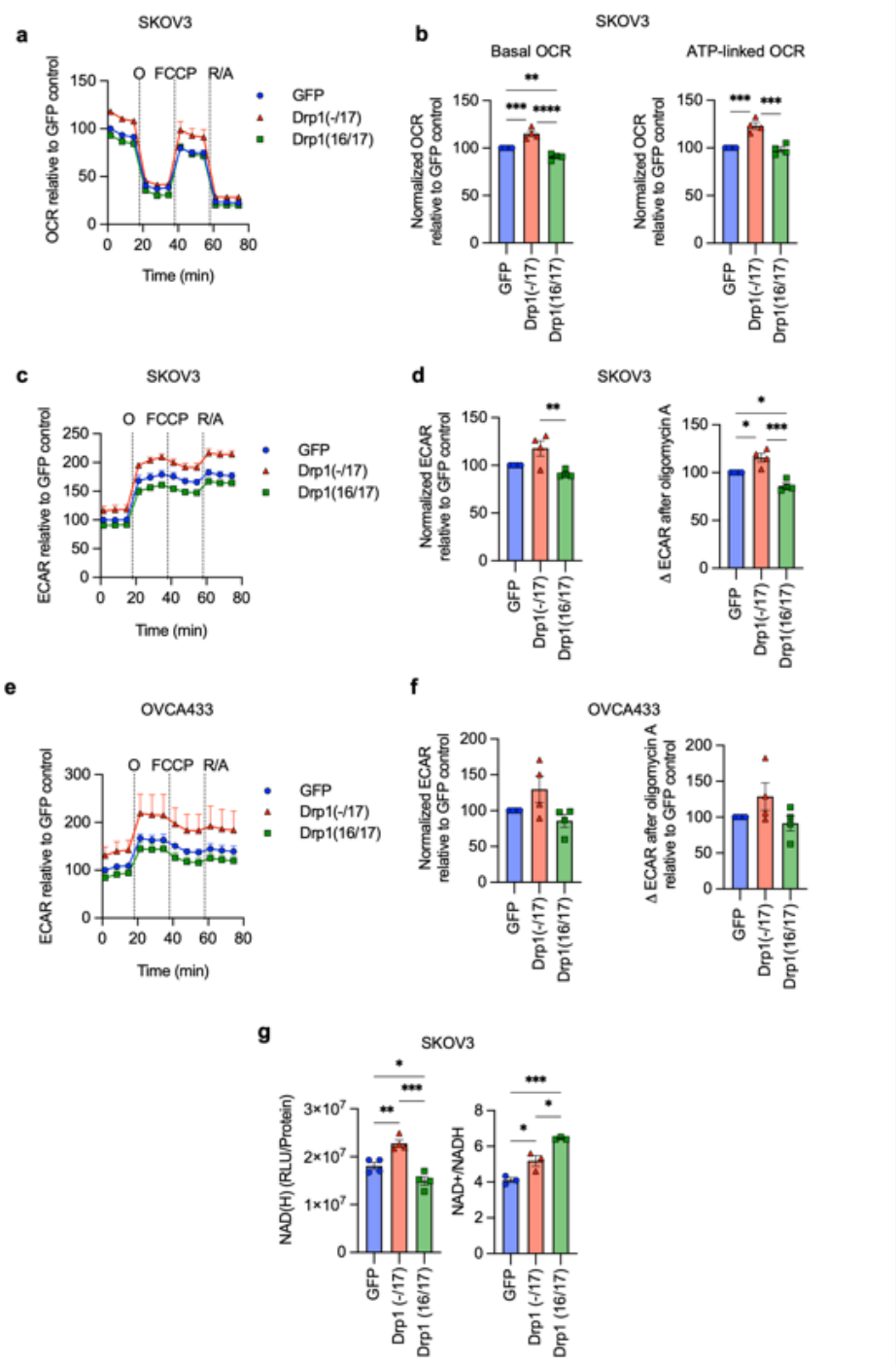

Extended Data Figure 7. Expression of Drp1(-/17) splice variant increases mitochondrial respiration in SKOV3 cells.

a. Expression of Drp1(-/17) increases oxygen consumption rates (OCR) in SKOV3 cells as assessed by mitochondrial stress test using Seahorse extracellular flux analysis (O: oligomycin A, R/A: rotenone/antimycin A; OCR is normalized to cell viability and expressed relative to GFP control, n=4)

b. Basal OCR and ATP-linked OCR are increased in cells expressing Drp1(-/17) compared to Drp1(16/17). Data are expressed relative to GFP control (n=4, one-way ANOVA Basal OCR $p<0.0001$; ATP-linked OCR $p=0.0001$; Tukey's post test *$p<0.05$, **$p<0.01$)

c. Extracellular acidification rates (ECAR) of SKOV3 cells expressing GFP control, Drp1(-/17) or Drp1(16/17). ECAR traces are derived in parallel to OCR values from mitochondrial stress test.
d. Basal ECAR and ΔECAR following oligomycin A inhibition of ATP-synthase were quantified in SKOV3 cells expressing GFP control, Drp1(-/17) or Drp1(16/17) (n=4, one-way ANOVA Basal ECAR p=0.0088; ΔECAR p=0.0003; Tukey's post test *p<0.05, **p<0.01, ***p<0.001).
e. ECAR traces from OVCA433 cells expressing GFP control, Drp1(-/17) or Drp1(16/17).
f. Basal ECAR and ΔECAR following oligomycin A inhibition of ATP-synthase were quantified in OVCA433 cells expressing GFP control, Drp1(-/17) or Drp1(16/17) (n=4, one-way ANOVA Basal ECAR p=0.0743; ΔECAR p=0.1501).
g. Total NAD(H) levels are increased in response to Drp1(-/17) expression relative to SKOV3 cells expressing GFP control or Drp1(16/17), while the ratio of NAD+/NADH is significantly decreased (one-way ANOVA NAD(H) n=4, p=0.0002; NAD+/NADH n=3 p=0.0004; Tukey's post test *p<0.05, ***p<0.001, ****p<0.0001).

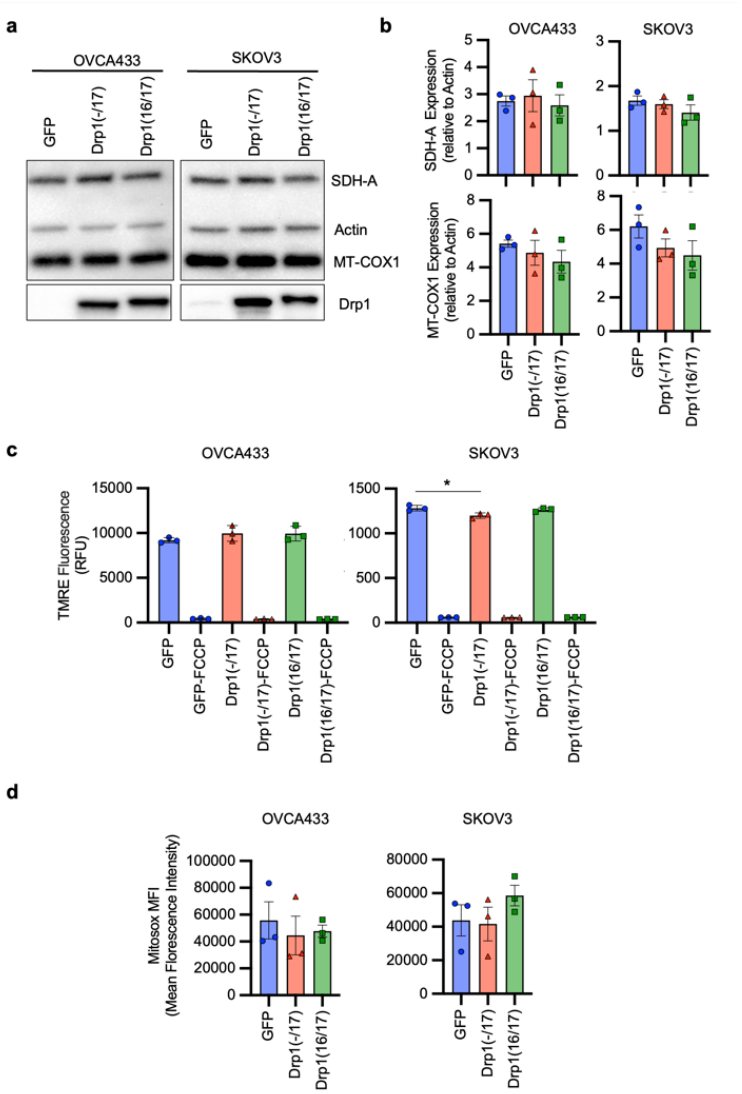

Extended Data Figure 8. Expression of Drp1 (-/17) or Drp1(16/17) does not affect protein levels of ETC components or mitochondrial membrane potential in ovarian cancer cells.

a. Levels of nuclear-DNA encoded SDH-A (Complex II) and mitochondrial-DNA encoded COX-1 (Complex IV) proteins are unchanged in both Drp1(-/17) and Drp1(16/17) expressing cells compared to GFP control cells. Data from one experimental replicate western blot is shown.

b. Quantification of SDH-A and MT-COX1 protein expression normalized to β-Actin in OVCA433 and SKOV3 cells by densitometry using ImageJ. (n=3, one-way ANOVA SDH-A expression; OVCA433 p=0.8407, SKOV3 p=0.3893, MT-COX1 expression; OVCA333 p=0. 4876, SKOV3 p=0. 2842).

c. Mitochondrial membrane potential was measured using TMRE (100nM) at baseline and with FCCP treatment (10 μM, 30 mins) in OVCA433 and SKOV3 cells expressing GFP control, Drp1(-/17) or Drp1(16/17) (n=3, one-way ANOVA of untreated cells OVCA433 p=0.3908, SKOV3 p=,0.0256, Tukey's post test *p=0.0264; one-way ANOVA comparison of FCCP treated cells OVCA433 p=0.3449, SKOV3 p=0.1715).

d. Drp1(-/17) and Drp1(16/17) overexpression in OVCA433 and SKOV3 cells did not alter MitoSox fluorescence, a mitochondrial targeted dye susceptible to superoxide mediated oxidation (n=3, one-way ANOVA OVCA433 p=0.7971, SKOV3=0.3830).

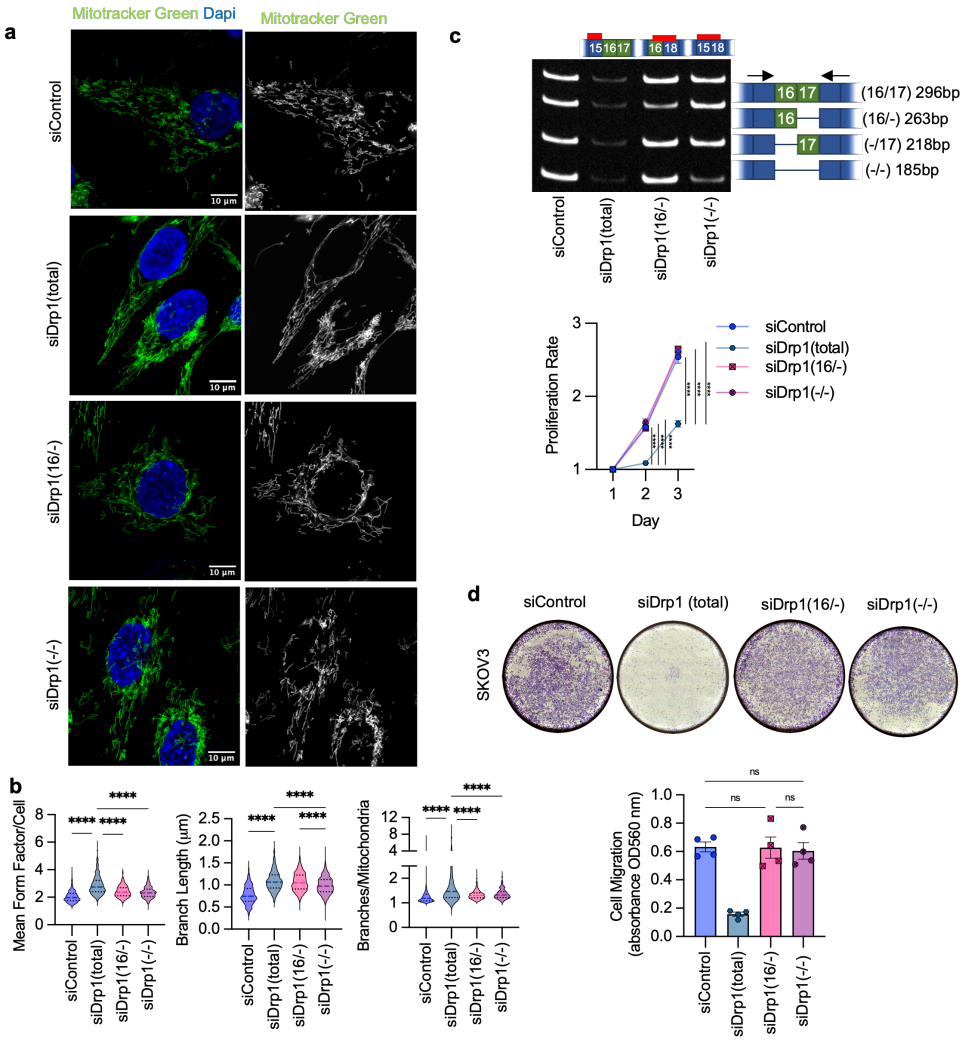

Extended Data Figure 9. Specific knock-down of endogenous Drp1(-/-) and Drp1(16/-) variants and effects on mitochondrial morphology, cell proliferation and migration.

a. Representative epifluorescence images of mitochondrial morphology upon splice variant specific siRNA Drp1 knockdown in SKOV3 cells. (Green: mitochondria stained with mitotracker green and Blue: DAPI). Scale bar: 10 µm.

b. Quantification of mitochondrial morphological represented by three independent descriptors as analyzed by mitochondria analyzer in ImageJ. (n = 560 cells from siControl, n = 334 cells from siDrp1(total), n=630 from siDrp1(16/17), n=655 from siDrp1(-/17) and n=555 from siDrp1(-/-)&(16/-) were analyzed. (one-way ANOVA Mean Form Factor p <0.0001; Branch Length p <0.0001 and Branches/mito p<0.0001. Tukey's post test was performed to assess differences between groups and analysis comparing groups to siDrp1(total) are shown, ****p <0.0001).

c. Drp1(-/-) and Drp1(16/-) variant specific knockdown did not alter cell proliferation in SKOV3 cells as no difference in proliferation rate compared to siControl cells. Cell proliferation was assessed by FluoReporter dsDNA quantification and proliferation rate expressed as increase in the cell density relative to day 1 (n=4, two-way ANOVA group factor variance p<0.0001, Tukey's post test ****p < 0.0001).

d. Cell migration was unchanged upon knock-down of Drp1(-/-) and Drp1(16/-) splice variants in SKOV3 cells. Post Drp1 knock-down, cell migration was assessed using the Boyden chamber transwell assay and quantified by measuring the absorbance of the crystal violet staining of migrated cells. Images are representative of 4 independent assays (n=4, one-way ANOVA ****p<0.0001. Tukey's post test was performed to assess differences between groups and analysis comparing siControl, siDrp1(16/17), siDrp1(-/17) and siDrp1(-/-)&(16/-) groups are shown).